Journal of Applied Fluid Mechanics, Vol. 19, No. 7, pp. 1676-1696, 2026.
Available online at www.jafmonline.net, ISSN 1735-3572, EISSN 1735-3645.
https://doi.org/10.47176/jafm.19.7.4172

Performance Estimation of Hybrid PV–Savonius Turbines Using Artificial Neural Networks and Computational Fluid Dynamics: Effects of Panel Position and Configuration on Turbine Aerodynamics

M. Yilmaz, Y. M. Yilmaz, and H. Yavuz†

Faculty of Engineering, Department of Mechanical Engineering, Çukurova University, 01330, Adana, Turkey

†*Corresponding Author Email: hyavuz@cu.edu.tr*

ABSTRACT

This study examines the aerodynamic performance of a Savonius-type vertical axis wind turbine integrated with photovoltaic panels that function simultaneously as flow deflectors. Two-dimensional transient simulations were performed using the k–ω Shear Stress Transport (SST) Unsteady Reynolds-Averaged Navier–Stokes (URANS) turbulence model to evaluate the influence of panel length (L), distance (x), and tilt angle (α) on the turbine's torque coefficient (C_m) and power coefficient (C_p). The configuration with $L = 2$ *m*, $x = 0.5$ *m*, and $\alpha = 35°$ achieved the highest aerodynamic efficiency, yielding a maximum power coefficient of $C_p = 0.3514$ at a tip speed ratio (TSR) of 1, representing an approximately 40.8% improvement over the baseline design. To minimize the number of required CFD simulations and enable performance prediction across untested configurations, Artificial Neural Network models are developed and trained using datasets obtained from the transient CFD analyses. The optimal Elman Neural Network model, employing five neurons with a *tansig* activation function and the *trainlm* learning algorithm, achieved high predictive accuracy with a Mean Absolute Percentage Error (*MAPE*) of 3.18%, Root Mean Square Error (*RMSE*) of 0.014, and Mean Absolute Error (*MAE*) of 0.0113. The developed ENN-based framework provides a computationally efficient and accurate alternative to CFD simulations, effectively capturing the nonlinear and time-dependent aerodynamic interactions of the turbine–panel system and supporting design optimization of hybrid renewable configurations.

Article History

Received November 15, 2025
Revised January 5, 2026
Accepted February 7, 2026
Available online May 8, 2026

Keywords:

Savonius turbine
Artificial neural network
Photovoltaic panel
Renewable energy
Computational fluid dynamics simulation

1. INTRODUCTION

Many countries are focusing on reducing the greenhouse gas emissions and addressing the climate change. As a result, the development and improvement of renewable energy systems have become critically important (Udochukwu & Innocent, 2024; Kut & Pietrucha-Urbanik, 2024). As reported by Sims et al. (2003), increasing the efficiency of renewable energy systems and adopting innovative designs and novel operational approaches are essential to achieve economic benefits and ensure long-term sustainability.

Türkiye, like many other countries, has been steadily increasing its investments in solar and wind-based renewable energy systems (Yüzer, 2023; Çakmak, 2024). The main objectives of these investments are to reduce dependency on imported fossil fuels, decrease the national carbon footprint and reduce energy-related risks, thereby improving energy security (Ozturk, 2013). As of September 2025, the installed capacities of solar and wind power plants in Türkiye have reached 24,090 MW and 13,884 MW, respectively (Enerji, 2025). In addition, government support for small-scale local systems has encouraged the widespread installation of rooftop photovoltaic (PV) systems on industrial and commercial buildings (IEEFA, 2019).

Among other major renewable energy sources, wind energy stands out as a widely utilized technology for sustainable power generation. Wind turbines, which convert the kinetic energy of wind into mechanical and subsequently electrical energy, are generally classified into two main categories based on their rotational axes: horizontal-axis wind turbines (HAWTs) and vertical-axis wind turbines (VAWTs) (Wenehenubun et al. 2015; Karimian & Abdolahifar, 2020). Among VAWTs, the Savonius turbine stands out as a drag-type configuration

NOMENCLATURE

A	swept area of the rotor	P_{wind}	wind power
ANN	Artificial Neural Network	*PV*	photovoltaic
C_m	torque coefficient	R^2	determination coefficient
CFD	Computational Fluid Dynamics	*RMSE*	Root Mean Square Error
C_p	power coefficient	*RNN*	Recurrent Neural Networks
D	rotor diameter	SST	Shear Stress Transport
Db	rotating domain diameter	*TI*	Turbulence Intensity
d	blade diameter	*TSR*, λ	Tip Speed Ratio
ENN	Elman Neural Network	*TVR*	Turbulence Viscosity Ratio
FNN	Feedforward Neural Network	U_∞	velocity inlet
GA	Genetic Algorithm	*URANS*	Unsteady Reynolds-Averaged Navier–Stokes
HAWT	Horizontal-axis wind turbine	*VAWT*	Vertical-Axis Wind Turbine
HWSES	Hybrid Wind-Solar Energy Systems	x	panel distance
L	panel length	y^+	dimensionless wall distance
MAE	Mean Absolute Erro	α	panel tilt angle
MAPE	Mean Absolute Percentage Error	ω	angular velocity of the rotor
M_t	torque produced by the turbine	θ	rotation angle per step
P_{output}	mechanical power		

known for its simple design, low manufacturing cost and reliable self-starting behavior (Rizk & Nasr, 2023; Akwa et al. 2012; Al-Ghriybah et al. 2021). The performance of Savonius turbines is influenced by factors such as blade number, aspect ratio, overlap ratio and blade shape (Dewan et al. 2021; Harsito et al. 2020).

Several studies have demonstrated that introducing deflectors can significantly improve Savonius turbine performance by guiding airflow toward the advancing blade and minimizing counteracting forces (Guo et al. 2020; Golecha et al. 2011; Sharma & Sharma, 2016). Mohamed et al. (2010) optimized deflector placement and achieved over a 27% increase in power coefficient (C_p) at specific tip speed ratios (*TSR*). In a subsequent study, Mohamed et al. (2011) combined optimized deflector positioning with an improved blade profile, resulting in a 38.9% increase in C_p at a *TSR* of 0.7. Similarly, Altan & Atılgan (2010) employed a deflector structure to prevent negative torque generation and accelerate airflow entering the rotor, leading to higher torque and power coefficients. Aboujaoude et al. (2022) also reported that an axisymmetric deflector design improved the turbine's C_p by approximately 25%, achieving a maximum value of 0.31 at *TSR* = 1. These findings highlight that the deflector geometry and placement are critical in enhancing turbine efficiency.

Rooftop PV systems have been widely adopted as cost-effective solutions for reducing energy expenses (Lee et al. 2014). However, in Türkiye, their effectiveness is strongly seasonal, most productive during late spring to early autumn, when solar irradiance is high and significantly reduced during winter when wind speeds are stronger. This seasonal imbalance suggests that hybridizing rooftop PV systems with small-scale wind turbines could provide more consistent energy generation. Lu et al. (2023) investigated a forward-facing step configuration to create a rooftop and then used a slanted PV panel on this step as a deflector. They reported that the PV panel provided only an additional 11.7% improvement over the step configuration, with 45° identified as the optimal tilt angle. Such configurations exemplify Hybrid Wind-Solar Energy Systems (HWSES), which combine PV panels and wind turbines to enhance reliability and mitigate the intermittency of standalone renewable systems (Zohuri, 2018; Ingole & Rakhond 2015).

While Computational Fluid Dynamics (CFD) simulations and experimental studies are essential tools for analyzing turbine aerodynamics, they are often time-consuming and computationally expensive (Mohammadi et al. 2018; Noman et al. 2023). This limitation has motivated researchers to explore data-driven approaches that can complement CFD analyses. Among these, Artificial Neural Networks (ANNs) have been increasingly used in renewable energy research for system modeling, performance estimation and optimization (Jha et al. 2017). For instance, Storti et al. (2019) used an ANN model trained on CFD data to optimize Savonius deflector geometry via a genetic algorithm, significantly reducing computational cost. Noman et al. (2023) developed an ANN-based virtual clone to predict the Savonius turbine's power coefficient, achieving over 98% fidelity. Similarly, Biswas et al. (2016) and Debnath & Das (2010) used ANN models to predict turbine performance under varying geometrical and operational conditions. Rathod et al. (2021) reported that ANN models outperformed genetic expression programming (GEP) in predicting turbine power coefficients ($R^2 \approx 0.97$ vs. 0.65).

Despite these advances, studies that use PV panels simultaneously as aerodynamic deflectors and power-generating components remain scarce. Lu et al. (2023) provided a valuable foundation by analyzing a PV–Savonius configuration, but their study was limited to a fixed panel length and position. The present work expands on this concept by systematically examining how variations in PV panel tilt angle, length and distance affect the aerodynamic performance of the Savonius turbine using transient CFD simulations. Furthermore, to reduce the number of required CFD simulations and to enable performance estimation for untested configurations, Artificial Neural Network (ANN) models are developed and trained using CFD-generated datasets. Feedforward Neural Networks (FNN) and Elman Neural Networks

(ENN) are employed and their predictive capabilities are evaluated through statistical performance metrics including Mean Absolute Error (MAE), Root Mean Square Error (RMSE) and Mean Absolute Percentage Error (MAPE).

The remainder of this paper is organized as follows. Section 2 introduces the numerical modeling framework, detailing the geometric configuration of the Savonius turbine, the arrangement of the photovoltaic (PV) panels and the definition of key study parameters. Section 3 presents the computational model, including the governing equations, computational domain, boundary conditions and mesh generation strategy. Section 4 describes the numerical procedure, covering the grid and time-step independence studies, as well as the validation of the computational model. Section 5 focuses on the Artificial Neural Network (ANN) methodology, outlining the Feedforward and Elman network architectures, transfer functions and performance evaluation metrics. Section 6 discusses the simulation outcomes and ANN prediction results, including the design of the optimal models, comparative assessments between network types and an analysis of the influence of PV panel configurations on the aerodynamic behavior and performance of the turbine. Finally, Section 7 summarizes the main findings and provides concluding remarks, along with recommendations for future work.

2. NUMERICAL MODELING AND CONFIGURATION FRAMEWORK

In this study, a solar panel inclined at various angles is analyzed numerically to investigate its function as a flow deflector and its influence on the aerodynamic performance of a Savonius-type wind turbine. Expanding upon the work by Lu et al. (2023), the present research systematically examines the effects of panel position, length and inclination on the flow characteristics and turbine performance parameters, including the moment coefficient (C_m) and power coefficient (C_p). The primary objective is to understand how the geometric arrangement of the PV panel modifies the local airflow and to quantify its influence on the hybrid system's efficiency.

The aerodynamic behavior of the system is evaluated through computational fluid dynamics (CFD) simulations. A two-dimensional unsteady Reynolds-averaged Navier–Stokes (URANS) approach with the k–ω turbulence model is employed to simulate the transient flow field around the turbine–panel configuration under different geometric and operational conditions. This modeling strategy, frequently adopted in the literature, provides a reliable balance between computational accuracy and efficiency when analyzing Savonius-type turbines. As emphasized by Duc et al. (2023), the two-dimensional URANS approach remains one of the most practical and well-validated methods for Savonius turbine studies, offering reasonable agreement with experimental data at a manageable computational cost.

Savonius turbines inherently exhibit three-dimensional flow characteristics, including complex vortex structures, spanwise flow development, and tip effects, which cannot be fully captured using two-dimensional simulations. Ferrari et al. (2017) quantified the influence of neglected three-dimensional effects by comparing 2D and 3D URANS simulations employing the k–ω SST turbulence model. At TSR = 0.58, the reported discrepancies were 14.32% for the torque coefficient (C_m) and 15.07% for the power coefficient (C_p), increasing to 19.8% and 20.47%, respectively, at TSR = 0.81. In the present study, the numerical predictions are validated against a wide range of published numerical and experimental results, with the maximum deviation from experimental measurements limited to approximately 5% for TSR values of 0.6 and 0.8. Although the two-dimensional URANS framework cannot reproduce all three-dimensional flow phenomena, it is capable of capturing reliable aerodynamic trends for comparative performance assessment. Moreover, its substantially reduced computational cost enables systematic parametric analysis, which would be computationally prohibitive using fully three-dimensional simulations. For these reasons, the two-dimensional URANS–SST k–ω model is deliberately adopted in this study.

The numerical results obtained from these simulations are subsequently utilized to ANN models for predicting turbine performance under untested configurations. By combining CFD and ANN approaches, the study aimed to estimate performance trends for a wide range of design parameters with a reduced number of CFD runs. This methodology enables efficient evaluation of multiple design alternatives, minimizing both computational cost and simulation time while preserving prediction accuracy.

2.1 Geometry of the Savonius Turbine and PV Panel Arrangement

The classical Savonius wind turbine geometry, shown in Fig. 1, consists of two semi-cylindrical blades. The advancing blade captures the incoming wind, producing positive torque, while the returning blade generates counteracting torque (Sagharichi et al. 2018; Bai et al. 2019).

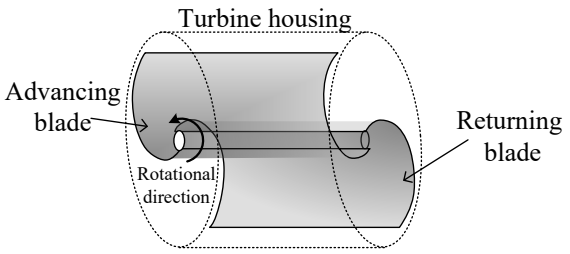


Fig. 1 Classical horizontal-axis Savonius wind turbine

A solar panel of length L is positioned at a distance x in front of the returning blade and inclined at an angle α, as illustrated in Fig. 2. The baseline turbine geometry follows previously reported models from both numerical (Nimvari et al. 2020; Tian et al. 2018) and experimental (Sheldahl et al. 1978) studies. The detailed parameters are summarized in Table 1, where the rotor diameter (D) is 0.909 m, the rotating domain diameter (D_b) is 0.999 m, the blade diameter (d) is 0.5 m and the overlap ratio (e/D) is 0.1 m.

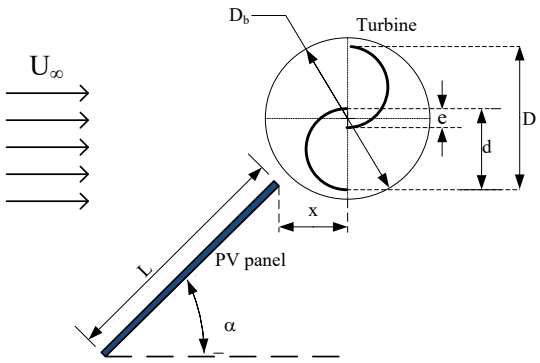


Fig. 2 Schematic of the Savonius wind turbine integrated with an inclined PV panel

Table 1 Turbine geometric parameters.

Savonius Turbine Parameters	Value
Rotor diameter (*D*)	0.909 m
Blade diameter (*d*)	0.5 m
Rotating Domain Diameter (D_b)	0.999 m
Overlap raito (*e*/*D*)	0.1 m

The hybrid configuration of the turbine and solar panel is shown in Fig. 3. In this arrangement, the turbine is mounted above the PV panel, which acts as a deflector to guide the incoming airflow toward the advancing blade. The deflected flow accelerates over the tilted panel, increasing the local wind velocity at the turbine inlet. This interaction enhances the aerodynamic torque generation and overall performance of the system.

A parametric study is conducted by varying the geometric and operational parameters of the PV–turbine system. As depicted in Fig. 4., the panel length (*L*), distance from the turbine (*x*) and tilt angle (*α*) are selected as the key geometric variables, while the tip-speed ratio (*TSR*) is considered as the main operational variable. These parameters collectively influence the local flow direction, velocity distribution and pressure gradients around the turbine.

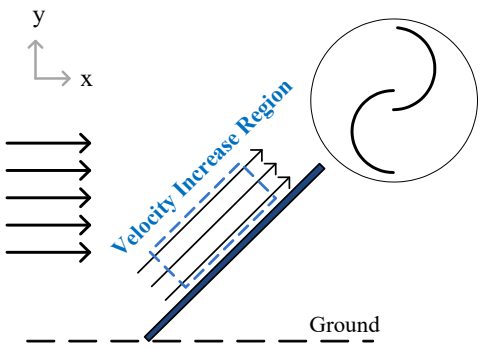


Fig. 3 Schematic of the hybrid wind–solar energy system (HWSES) illustrating airflow acceleration and deflection

The parameter ranges are selected as follows:

- Panel length (*L*): 1 m, 1.5 m and 2 m
- Distance from turbine (*x*): 0.5 m, 1.0 m and 1.5 m
- Tilt angle (*α*): 30°, 35° and 40°
- Tip-speed ratio (*TSR*): 0.6, 0.8, 1.0 and 1.2

This configuration resulted in 3×3×3×4 = 108 CFD cases, covering a wide range of practical conditions. The resulting data are used as input and target datasets for ANN model training and testing.

While the present study focuses on panel length, panel–turbine distance and tilt angle due to their dominant influence on flow deflection and Savonius turbine aerodynamics (Fig. 4), additional practical parameters such as panel width, turbine height, and three-dimensional geometrical effects may also affect the overall system performance. Investigation of these parameters is recommended in future studies to extend the applicability of the proposed hybrid configuration to realistic three-dimensional and urban renewable energy installations.

2.2 Parameter Definitions of the Study

The geometric and operational parameters are chosen based on practical feasibility and their influence on the aerodynamic interaction between the PV panel and the

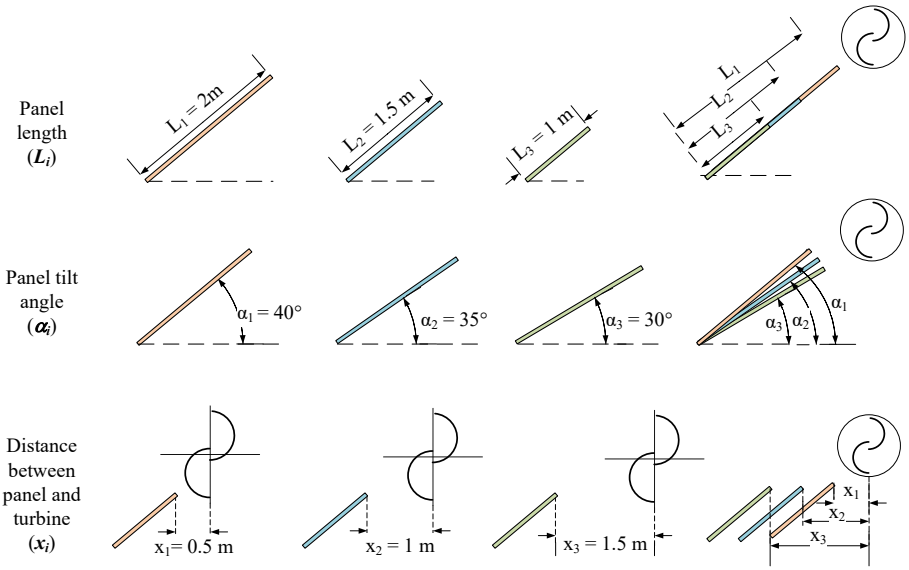


Fig. 4 Definition of the geometric parameters used to describe the PV panel configuration, including panel length (L_i), tilt angle (α_i), and panel-to-turbine distance (x_i)

Savonius turbine. The panel lengths (L) of 1 to 2 m are selected to reflect typical residential and light-industrial solar modules, which usually range from 1 m to 1.7 m, with larger models extending beyond 2 m (Deye ESS, 2025).

The distance between the panel and turbine (x) is determined by considering both aerodynamic interaction and mechanical clearance. The minimum spacing of 0.5 m ensures that the deflected flow interacts efficiently with the turbine without physical interference, while a distance of 1.5 m represents a configuration where aerodynamic influence begins to weaken. These dimensions are also compatible with commonly available commercial panel sizes and facilitate the practical installation and applicability of hybrid systems.

Based on established photovoltaic and aerodynamic studies, the tilt angle of the panel (α) was varied between 30° and 40°. Kacira et al. (2004) investigated optimal photovoltaic inclination over a wide angular range (0°–60°) and reported that tilt angles between 30° and 40° provide favorable year-round performance by balancing seasonal variations in solar irradiation. Similar optimal inclination ranges have been reported for regions such as Türkiye, North Africa, and Southern Europe (Yadav & Chandel, 2013), as illustrated in Fig. 5 (World Map Wallpapers, 2025). From an aerodynamic perspective, studies on Savonius turbines equipped with deflectors or inclined guiding surfaces indicate that moderate inclination angles improve flow redirection toward the advancing blade while limiting flow separation and adverse pressure gradients associated with larger angles. Comparable sensitivity of aerodynamic loading and flow response to inclination has also been reported for wind energy structures with inclined or high-aspect-ratio components (Li et al. 2025a). Therefore, the selected tilt angle range represents a practical and physically meaningful compromise that supports both effective aerodynamic flow control and photovoltaic performance.

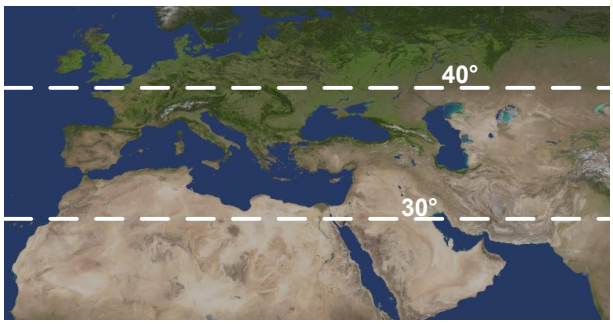


Fig. 5 Map showing the optimal solar panel tilt angle range (30°–40°) across different regions

3. COMPUTATIONAL MODEL

The aerodynamic performance of the Savonius-type turbine integrated with a photovoltaic (PV) panel is investigated using an incompressible Unsteady Reynolds-Averaged Navier–Stokes (URANS) approach with the SST k–ω turbulence model. The computational domain consisted of two regions: a rotating zone containing the turbine and a stationary outer flow region. A uniform velocity inlet of 7 m/s is applied with a turbulence intensity (TI) of 1% and a turbulence viscosity ratio (TVR) of 10, while a pressure outlet condition with TI = 5% and TVR = 10 is defined at the outlet. The turbine blades are modeled as moving walls, rotating at a prescribed angular velocity corresponding to the selected *TSR*. Air is used as the working fluid, assuming constant density ($1.225\ kg/m^3$) and dynamic viscosity ($1.789\times10^{-5}\ kg/m{\cdot}s$), corresponding to a Reynolds number of 1×10^5.

The simulations are performed as transient analyses using a pressure-based solver. The angular velocity is computed for each *TSR* value. For *TSR* = 1, the calculated angular velocity is $\omega = 15.4015\ rad/s$, which corresponded to a time-step size of 0.001133 s, equivalent to a 1° rotor rotation per step. Each simulation covered 15 complete revolutions of the rotor and the results from the final revolution are used for performance evaluation to ensure steady periodic behavior.

The SIMPLE algorithm is employed for pressure–velocity coupling. The Second-Order Upwind scheme is applied for momentum discretization and the Least Squares Cell-Based method is used for gradient evaluation. Pressure and momentum relaxation factors are set to 0.3 and 0.4, respectively. The convergence is achieved when all residuals dropped below 10^{-6}. The final mesh has an average skewness of 0.08 and an orthogonal quality of 0.97, ensuring reliable numerical accuracy.

3.1 Governing Equations

The key non-dimensional parameters used to assess turbine performance include the power coefficient (C_p) and the torque coefficient (C_m), which reflect the turbine's ability to convert wind energy into mechanical output (Bai et al. 2019; Sobhani et al. 2017). The Tip Speed Ratio (*TSR*, or λ), representing the ratio between the blade tip speed and the incoming wind speed, is defined as:

$$\lambda = \frac{\omega R}{U_\infty} \tag{1}$$

where ω is the angular velocity (rad/s), R is the rotor radius (m) and U_∞ is the free-stream velocity (m/s).

The torque coefficient (C_m) is expressed as:

$$C_m = \frac{M_t}{0.5\rho A U_\infty^2 R} \tag{2}$$

where M_t is the torque produced by the turbine ($N.m$), ρ is the air density (kg/m^3) and A is the swept area (m^2).

The power coefficient (C_p), which measures the efficiency of mechanical power extraction, is given by:

$$C_p = \frac{P_{output}}{P_{wind}} = \frac{P_t}{0.5\rho A U_\infty^3} = \lambda C_m \tag{3}$$

The relationship between the rotation angle per time-step and angular velocity is given by:

$$\Delta t = \frac{\Delta\theta}{\omega} \tag{4}$$

$$\Delta\theta = \frac{\theta\pi}{180} \tag{5}$$

where Δt is the time-step (s) and θ is the rotation angle (°).

For an incompressible Newtonian fluid, the time-averaged continuity and momentum equations are expressed as:

$$\frac{\partial \bar{u}_i}{\partial x_i} = 0, \quad \frac{\partial \bar{u}_i}{\partial t} + \bar{u}_j \frac{\partial \bar{u}_i}{\partial x_j} = -\frac{1}{\rho}\frac{\partial \bar{p}}{\partial x_i} + \nu \frac{\partial^2 \bar{u}_i}{\partial x_j^2} - \frac{\partial \rho \overline{u_i' u_j'}}{\partial x_j} \tag{6}$$

The term $\partial(-\rho\overline{u_i'u_j'})/\partial x_j$ is called the Reynolds stress term,which must be modeled to close the above equations.

The URANS approach combined with the k–ω SST model provides an efficient and sufficiently accurate method to capture the unsteady aerodynamic behavior of Savonius turbines (Duc et al. 2023). The model introduces two additional transport equations for the turbulent kinetic energy (k) and specific dissipation rate (ω):

$$\frac{\partial(\rho k)}{\partial t} + \frac{\partial(\rho \bar{u}_j k)}{\partial x_j} = P_k - \beta^* \rho k\omega + \frac{\partial}{\partial x_j}\left[(\mu + \sigma_k \mu_t)\frac{\partial k}{\partial x_j}\right] \tag{7}$$

$$\frac{\partial(\rho\omega)}{\partial t} + \frac{\partial(\rho \tilde{u}_j \omega)}{\partial x_j} = P_\omega - D_\omega + S_\omega$$

$$P_\omega = \alpha \frac{\omega}{k} P_k - \beta\rho\omega^2 \tag{8}$$

$$D_\omega = \frac{\partial}{\partial x_j}\left[(\mu + \sigma_\omega \mu_t)\frac{\partial \omega}{\partial x_j}\right]$$

$$S_\omega = 2(1-F_1)\rho\sigma_{\omega 2}\frac{1}{\omega}\frac{\partial k}{\partial x_j}\frac{\partial \omega}{\partial x_j}$$

where P_ω, D_ω and S_ω denote the production, diffusion and cross-diffusion terms of ω. In the SST model, μ and μ_t represent the molecular and turbulent viscosities, P_k denotes the turbulent kinetic energy production term and F_1 is the blending function used to switch between the k–ω and k–ε formulations. The turbulent (eddy) viscosity is computed as:

$$\mu_t = \frac{\rho k}{\omega} \tag{9}$$

3.2 Computational Domain and Boundary Conditions

The computational domain is designed to ensure that boundary effects did not influence the flow field around the turbine. As illustrated in Fig. 6, the domain is divided into two main zones: a rotating subdomain enclosing the turbine and a stationary external flow region (Tartuferi et al. 2015). The upstream length is set to 13D and the downstream wake region to 23D. The vertical boundaries are placed at 18D on the upper side and 1.6D on the lower side relative to the turbine center.

A velocity inlet (U_∞) boundary condition of 7 m/s in the x-direction is applied at the domain entrance, while an atmospheric pressure condition is assigned to the outlet (Lu et al. 2023; Nimvari et al. 2020).The upper boundary is modeled as a symmetry and the bottom surface, including the PV panel, is set as a stationary wall. The rotating region is modeled using a moving reference frame to account for the turbine's dynamic rotation.

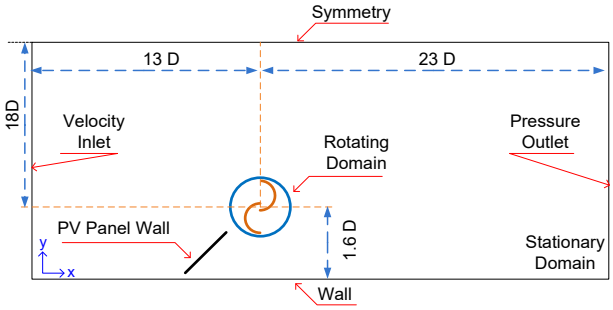


Fig. 6 Schematic representation of the computational domain and applied boundary conditions

3.3 Mesh Generation

Accurate mesh generation is critical for resolving the unsteady flow characteristics around the Savonius turbine and PV panel. Edge sizing is applied along the inner and outer blade surfaces and the wall boundaries to ensure high local resolution. Inflation layers (25 in total) are generated near the blades to capture the boundary layer accurately, with a uniform growth rate of 1.1 between adjacent layers.

In the present study, the first inflation layer thickness was set to 0.04 mm, ensuring sufficient near-wall resolution for the SST k–ω turbulence model. The near-wall resolution is verified by maintaining y^+ values below 1, with average and maximum values of approximately 0.4 and 0.9, respectively, indicating adequate resolution of the viscous sublayer. Detailed post-processing confirmed that y^+ values remain well below 1 over all blade surfaces and within the rotating domain. The reported y^+ statistics are vertex-based, providing a conservative assessment of near-wall resolution. Specifically, y^+ values range from 0.0268 to 0.882 on the lower blade and from 0.0321 to 0.5813 on the upper blade, with similar maximum values observed in the rotating domain (Fig. 6) adjacent to the blades. These results demonstrate adequate boundary layer resolution in regions of high curvature and flow separation. The overall mesh exhibited excellent quality, with low skewness and high orthogonal metrics, ensuring solution stability. The overall mesh geometry is shown in Fig. 7.

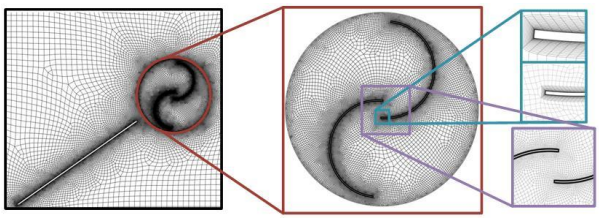


Fig. 7 Overall view of the mesh geometry used in the CFD simulations

Table 2 Characteristics of the three mesh configurations for the hybrid system

Mesh Density	Coarse	Medium	Fine
Total Number of Elements	188416	202475	230846
Number of Inflations	20	25	30
First Layer Thickness (mm)	0.06	0.04	0.02
Average Orthogonal Quality	0.97078	0.97284	0.97825
Average Skewness	0.0856	0.0862	0.0972
Average Aspect Ratio	5.006	4.732	4.285
Cm	0.354118	0.351461	0.351066

4. NUMERICAL PROCEDURE

Before the simulation results are analyzed or used for network training, it is essential to confirm that the computational setup provides consistent and physically reliable predictions. Therefore, the numerical procedure includes three verification stages: the grid independence test, the time-step independence test and model validation against published data.

4.1 Grid Independence Study

A grid-independence analysis is conducted at a tip speed ratio (*TSR*) of 1, as summarized in Table 2 and Fig. 8. Three mesh densities, coarse, medium and fine, containing 165 464, 184 182 and 212 294 elements, respectively, are compared using mesh-quality indicators such as average orthogonal quality, skewness and aspect ratio. Their effect on the torque coefficient (C_m) is also examined.

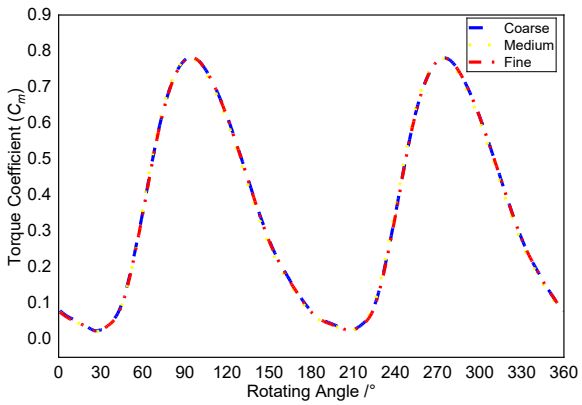


Fig. 8 Grid-independence study for the hybrid system

The sensitivity of the numerical results to mesh density near the PV panel surface was evaluated as part of the overall mesh independence study. Surface mesh sizes of 1 mm, 2 mm, and 3 mm were examined in the panel-adjacent region. The resulting variations in the predicted torque coefficient were found to be negligible, with no discernible impact on the overall aerodynamic performance trends or flow-field structures induced by the panel. Accordingly, a panel surface mesh size of 2 mm was adopted for all simulations, providing sufficient accuracy while avoiding unnecessary computational cost.

The difference in C_m between the coarse and medium meshes is 0.002657, while the difference between the medium and fine meshes is only 0.000395, indicating that further refinement caused negligible variation. Although Table 2 lists only average values, the minimum orthogonal quality exceeded 0.3 and the maximum skewness remained below 0.7 in all cases, confirming adequate numerical accuracy.

When compared with the findings of Nimvari et al. (2020), the fine mesh produced the closest agreement with the published torque-coefficient data. However, since the medium-density mesh satisfied both accuracy and computational-efficiency requirements, it is selected for the remaining analyses.

4.2 Time Step Independency Study

All CFD simulations are run for 15 complete rotor revolutions and the aerodynamic coefficients obtained from the final (converged) revolution are used for analysis (Fig. 9). To verify time-step independence, simulations are carried out using rotational increments of 0.5°, 1° and 1.5° per iteration. The corresponding time-step (Δt) is calculated from the turbine's rotational speed using Eqs. (4) and (5).

Comparisons of the instantaneous C_m over a full revolution (Fig. 10) revealed nearly identical results for all angular increments, confirming temporal convergence. Quantitatively, the C_m difference between 0.5° and 1° is below 0.04 and between 1° and 1.5° below 0.03, indicating that additional reduction of the time-step would not improve accuracy meaningfully.

Considering both precision and computational cost, a rotational increment of 1° per iteration is selected as the nominal time-step for the remainder of the simulations. This step size provides reliable rotor-performance predictions while keeping total simulation time within reasonable limits.

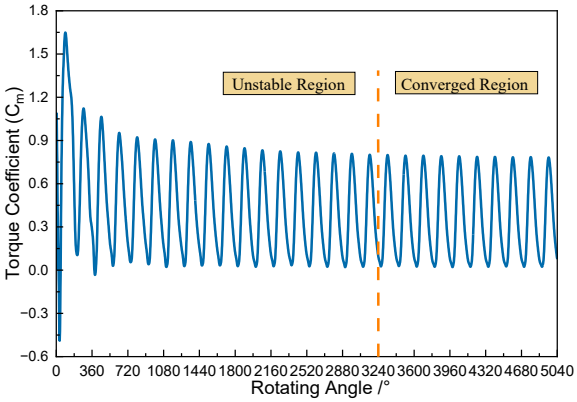


Fig. 9 Variation of torque coefficient (C_m) over 15 rotor revolutions at *TSR = 1* for the hybrid system

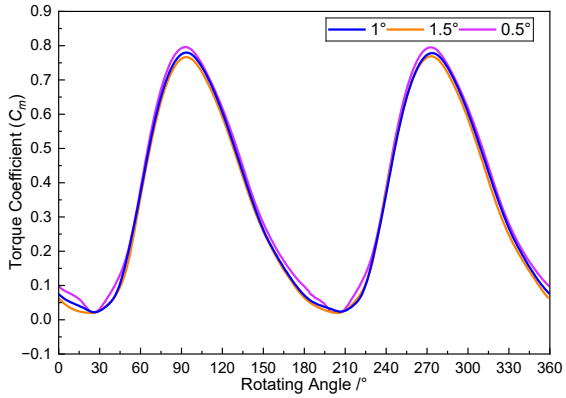


Fig. 10 Time-step independence results for the hybrid system

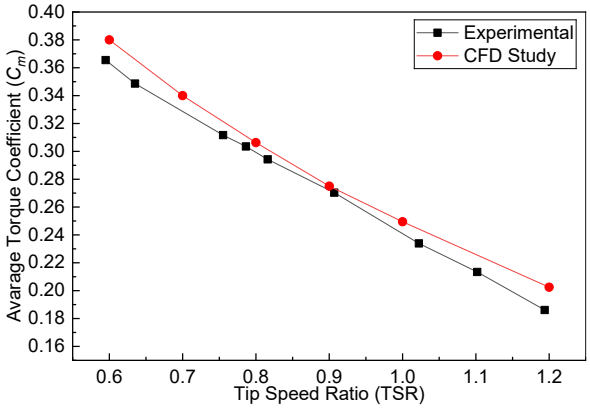


Fig. 11 Comparison of calculated C_m values with experimental results at various TSR values

4.3 Validation

For validation, the turbine model is simulated without the PV panel at several *TSR* values. The calculated C_m values are compared with the experimental data of Sheldahl et al. (1978). The comparison demonstrates close agreement with the measurements (Fig. 11), confirming that the computational model can accurately predict the aerodynamic performance of the Savonius turbine under similar operating conditions. Additionally, a comparison of the predicted power coefficient (C_p) with the literature results (Table 3) showed a maximum deviation of 4.82% at different TSR values, confirming the reliability and accuracy of the numerical model employed in this study.

The validation presented in this study is based on previously published experimental data for conventional Savonius turbines, as dedicated experimental measurements corresponding exactly to the present hybrid PV–Savonius geometry are not available. Consequently, the validation primarily confirms the numerical model's ability to capture the fundamental aerodynamic trends governing the torque coefficient (C_m) and power coefficient (C_p), rather than providing a geometry-specific experimental verification.

5. ARTIFICIAL NEURAL NETWORKS

Artificial Neural Networks (ANNs) are computational models inspired by the information-processing mechanism of the human brain. They consist of interconnected layers of artificial neurons that transmit and process data through weighted links. By learning relationships among multiple input parameters, ANNs can predict output variables in systems where analytical or statistical methods are impractical (Ünal et al. 2025).

Due to their capacity to represent nonlinear and complex relationships, ANNs have been effectively applied to various engineering problems (Ghorbani et al. 2013; Bilgili et al. 2023). A typical ANN architecture includes three main layers: an input layer, one or more hidden layers and an output layer. These layers are interconnected through weighted connections that enable signal propagation and learning (Fig. 12). Depending on their structure, they can be broadly categorized into feedforward neural networks (FNNs) and recurrent neural networks (RNNs) (Ghorbani et al. 2017; Tümse et al. 2022a). The Elman neural network (ENN) is a specific type of recurrent network distinguished by its internal feedback connections (Cacciola et al. 2012; Chandra & Zhang, 2012).

In many engineering applications, performing CFD analyses for every geometric configuration is both computationally demanding and time-consuming. Therefore, in this study, ANNs are employed to approximate the outcomes of CFD simulations, substantially reducing computational cost and time while maintaining acceptable accuracy (Sanaye et al. 2025).

The output of the network is obtained through nonlinear interactions between input variables and their associated connection weights, as expressed by Eq. (10). In this formulation, F represents the predicted value; w_{ij} and v_j denote the connection weights of the input and hidden layers, respectively; b_j is the bias term; and x_i corresponds to the input variables. The parameters h and k represent the number of neurons in the hidden layer and the number of input parameters, respectively.

$$F = f\left(a + \sum_{j=1}^{h} v_j \left[\sum_{i=1}^{k} w_{ij} x_i + b_j \right] \right) \tag{10}$$

Table 3 Comparison of power coefficient (C_p) between numerical and experimental results

Study	Turbulence Model	TSR= 0.6	TSR= 0.8	TSR= 1	C_p
		C_p			Maximum difference (%)
Present study	k–ω SST	0.228	0.2449	0.2494	-
Nimvari et al. (2020)	k–ω SST	0.2170	0.2374	0.2480	4.82
Tian et al. (2018)	k–ω SST	0.219	0.2398	0.247	3.94
Shaldl et al. (1978)	Experimental	0.2180	0.23944	0.2406	4.38

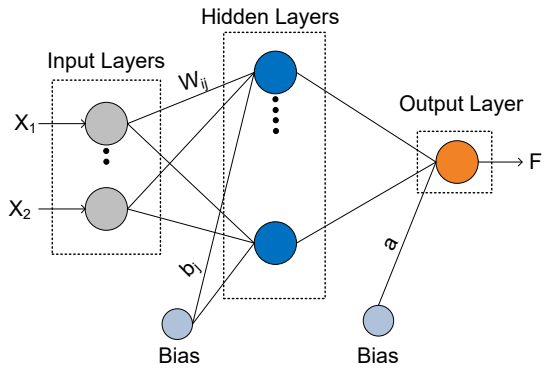


Fig. 12 Schematic structure of an artificial neural network (ANN)

In this study, the aerodynamic influence of varying the geometric configuration of a photovoltaic (PV) panel positioned in front of a Savonius turbine is investigated. A total of 108 distinct configurations are simulated to assess the aerodynamic interactions between the panel and turbine. The resulting dataset is divided into two subsets: 76 samples for training and 32 for testing the ANN models.

To evaluate and improve the predictive capability of ANN models, two different architectures, Elman Neural Network (ENN) and Feedforward Neural Network (FNN), are examined. For both networks, the tangential sigmoid (tansig) and logarithmic sigmoid (logsig) activation functions are tested in the hidden layers. Two training algorithms, Levenberg–Marquardt (trainlm) and Scaled Conjugate Gradient (trainscg), are used during network training.

The number of neurons in the hidden layer, activation function type and training algorithm are systematically varied to assess their influence on model performance. Each configuration is evaluated using statistical error metrics (MAPE, RMSE and MAE). The final network structures are selected based on the configurations that yielded the lowest error values for each ANN type.

5.1 Feedforward: Neural Network

The Feedforward Neural Network (FNN) represents the most fundamental ANN architecture, where information flows unidirectionally, from the input layer through the hidden layer(s) to the output layer, without any feedback connections. The multilayer FNN structure can approximate nonlinear relationships within the data to a certain extent.

In the present study, the FNN model utilized four input parameters: panel length, the distance between the panel and turbine, the panel tilt angle and the tip speed ratio (TSR). To examine the effect of network size, the number of neurons in the hidden layer is varied from 2 to 10. For each case, two activation functions (logsig and tansig) and two training algorithms (*trainlm* and *trainscg*) are applied. The performance of each combination is then evaluated to identify the configuration providing the most accurate prediction.

5.2 Elman Neural Network

The Elman Neural Network (ENN) is a type of recurrent network that extends the feedforward architecture by introducing feedback connections between layers. It contains an additional context layer that stores the previous hidden-layer outputs and reintroduces them into the network during subsequent iterations. This feedback mechanism enables the ENN to capture temporal or sequential dependencies within the data, making it well-suited for dynamic and nonlinear problems.

The ENN model employs the same input parameters as the FNN model such as panel length, panel–turbine distance, panel tilt angle and *TSR*. The number of neurons in the hidden layer is again varied between 2 and 10 and the same activation functions (*logsig* and *tansig*) and training algorithms (*trainlm* and *trainscg*) are tested. Maintaining identical input sets and training conditions for both models ensured a fair and consistent comparison between FNN and ENN architectures.

5.3 Transfer Functions

Transfer functions, also referred to as activation functions, define the output of a neuron based on its weighted input. These functions introduce nonlinearity into the model, allowing the network to capture complex, multidimensional relationships between inputs and outputs. In this study, two widely used activation functions, tangential sigmoid (tansig) and logarithmic sigmoid (logsig), are employed to evaluate their influence on prediction accuracy (Akbiyik & Yavuz, 2021; Tümse et al. 2022b).

The *tansig* function (Fig. 13a) maps input values to the range of [−1, 1] and is often preferred in hidden layers due to its balanced output and stable gradient behavior. It is expressed as:

$$\text{tansig}(a) = \frac{2}{1+e^{-2a}} - 1 \tag{11}$$

The logsig function (Fig. 13b), also known as the logistic sigmoid, maps inputs to [0, 1] and is typically used in output layers, particularly for normalized prediction or classification tasks. It is defined as:

$$\text{logsig}(a) = \frac{1}{1+e^{-a}} \tag{12}$$

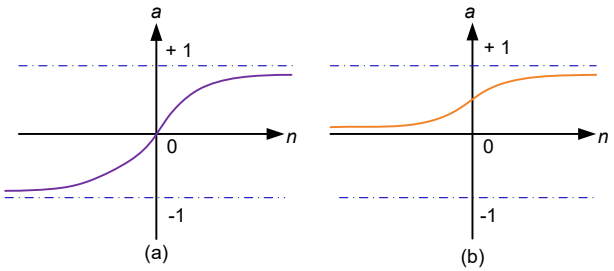


Fig. 13 Activation functions used in the ANN: (a) tangential sigmoid, (b) logarithmic sigmoid

5.4 Error Metrics

As noted by Chai & Draxler (2014), no single metric can fully represent model error characteristics; hence, multiple complementary metrics should be considered for a balanced evaluation. Root Mean Square Error (RMSE) is more sensitive to large deviations, Mean Absolute Error (MAE) indicates the average deviation magnitude and Mean Absolute Percentage Error (MAPE) expresses the error as a percentage of the actual value.

In this study, RMSE, MAE and MAPE are used collectively to assess the prediction accuracy and generalization performance of both ENN and FNN models. These metrics enable detailed evaluation by comparing predicted outputs with CFD-based reference data, providing a comprehensive understanding of model reliability (Willmott & Matsuura, 2005; Chai & Draxler, 2014).

The MAE, RMSE and MAPE are defined as follows:

$$\mathrm{MAE} = \frac{1}{N}\sum_{i=1}^{N}\left|y_i - \hat{y}_i\right| \tag{13}$$

where y_i and $\hat{y}_i$ represent the actual values and predicted values, respectively and N denotes the total number of data samples.

The Root Mean Square Error (RMSE) quantifies the standard deviation of prediction errors and penalizes larger deviations more strongly than MAE:

$$\mathrm{RMSE} = \sqrt{\frac{1}{N}\sum_{i=1}^{N}\left(y_i - \hat{y}_i\right)^2} \tag{14}$$

Finally, the Mean Absolute Percentage Error (MAPE) expresses the average absolute prediction error as a percentage of the actual values, providing a normalized measure of prediction accuracy:

$$\mathrm{MAPE} = \frac{100}{N}\sum_{i=1}^{N}\left|\frac{y_i - \hat{y}_i}{y_i}\right| \tag{15}$$

Lower values of these metrics indicate better prediction capability and generalization performance. The optimal configurations of the ENN and FNN architectures are determined by selecting the combination of neurons, activation functions and training algorithms that minimized these error values, resulting in the most efficient and accurate predictive models for the hybrid turbine system.

6. RESULT AND DISCUSSION

This section presents the findings of the computational analyses and artificial neural network (ANN) evaluations. The results are discussed in two main parts. The first part focuses on the design, optimization and comparative assessment of the FNN and ENN models, emphasizing their prediction accuracy and generalization performance across the tested datasets. The second part investigates the aerodynamic behavior of the Savonius turbine under different photovoltaic (PV) panel configurations, with particular attention to how variations in panel orientation and placement affect the torque and power coefficients of the hybrid system. Together, these analyses aim to provide a consistent interpretation of the numerical and ANN-based outcomes, supporting the evaluation of the most suitable configuration and modeling strategy for the proposed hybrid system.

6.1 The Optimum ENN Model

The performance of the ENN developed for predicting the torque coefficient (C_m) is evaluated under various configurations using different activation functions (*logsig* and *tansig*), training algorithms (*trainlm* and *trainscg*) and hidden neuron numbers (*N=2 to 10*). The results of these tests are summarized in Table 4, where the Mean Absolute Percentage Error (MAPE), Root Mean Square Error (RMSE) and Mean Absolute Error (MAE) are used as performance metrics to assess the accuracy of each configuration. As shown in Table 4, the configuration employing the *tansig* activation function with the *trainlm* algorithm and five neurons in the hidden layer (*N=5*) achieved the lowest error metrics. For this optimal model, the MAPE, RMSE and MAE are obtained as 3.1863%, 0.014 and 0.0113, respectively. These small errors indicate a close agreement between the predicted and reference CFD values of C_m. The results confirm that the *tansig* activation function, when combined with the Levenberg–Marquardt training algorithm, provides a strong nonlinear mapping capability suited for the aerodynamic data of this study. Thus, the selected ENN configuration balances predictive accuracy and computational efficiency while maintaining robust generalization performance.

Table 4 Performance metrics of various ENN models for C_m prediction

N	MAPE (%)				RMSE				MAE			
	Logsig		Tansig		Logsig		Tansig		Logsig		Tansig	
	trainlm	trainscg	trainlm	trainscg	trainlm	trainscg	trainlm	trainscg	trainlm	trainscg	trainlm	trainscg
2	5.5	7.3252	5.5002	9.165	0.0328	0.0337	0.0328	0.0393	0.0172	0.0239	0.0172	0.0308
3	6.5771	7.2089	5.4986	7.9254	0.0322	0.0314	0.0327	0.0336	0.0209	0.0241	0.0170	0.0263
4	3.9087	7.4492	4.1957	5.5633	0.0174	0.0346	0.0188	0.0227	0.013	0.0242	0.0139	0.0193
5	5.3842	7.6523	3.1863	6.4436	0.0283	0.034	0.014	0.0273	0.017	0.0254	0.0113	0.0219
6	3.8532	6.203	3.2252	5.1883	0.0177	0.0258	0.0176	0.022	0.0133	0.0211	0.0125	0.0185
7	5.5083	6.7788	4.8648	5.6004	0.029	0.0286	0.0243	0.0219	0.0178	0.0234	0.0174	0.019
8	8.3131	6.8275	6.9405	7.692	0.0506	0.0301	0.0371	0.0322	0.0295	0.022	0.0281	0.0256
9	9.358	8.2106	7.7934	7.0101	0.0417	0.0383	0.0361	0.0297	0.0301	0.027	0.0277	0.0249
10	10.855	7.4799	5.4446	6.0504	0.041	0.032	0.0235	0.0254	0.0352	0.0257	0.0202	0.0207

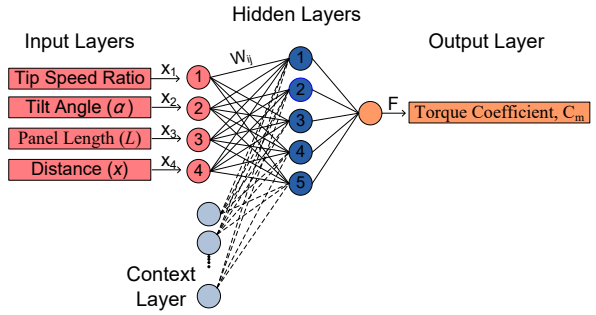


Fig. 14 Architecture of the Elman Neural Network (ENN) model developed for C_m prediction

The architecture of the optimized ENN model is shown schematically in Fig. 14. The network consists of four input parameters, Tip Speed Ratio (*TSR)*, panel tilt angle (α), panel length (L) and distance between the panel and turbine (x), which represent the dominant aerodynamic and geometric factors affecting turbine performance. A hidden layer processes these inputs through weighted connections (W_{ij}), enabling nonlinear transformation between the input and output spaces. ENN also includes a context layer that stores the hidden layer's outputs from the previous time step and feeds them back into the network. This recurrent feedback provides short-term memory, allowing the ENN to capture temporal or sequential dependencies that can arise from interacting flow phenomena in the CFD dataset. The output layer then produces the predicted torque coefficient (C_m) for each input configuration. The relationship between the ENN-predicted and actual C_m values is presented in Fig. 15. The regression analysis yields a coefficient of determination R^2=*0.9811*, indicating that the model explains over 98% of the variance observed in the CFD data. The regression line, *y=0.929x+0.0192*, lies close to the 1:1 reference, confirming strong agreement between the ENN predictions and CFD results. The high coefficient ($R^2 \approx 0.99$) further validates the ENN's reliability in mapping the nonlinear relationships among the aerodynamic variables (Tümse et al. 2022b).

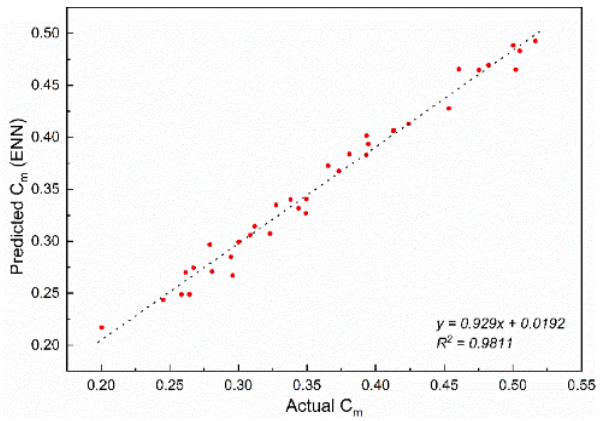


Fig. 15 Regression analysis of predicted versus actual C_m values for the ENN model (test dataset)

A further comparison between ENN-predicted and CFD-computed C_m values for different geometric configurations is presented in Fig. 16. The figure illustrates results for a fixed panel length (L=*1.5m*) with three inclination angles (α=*30°, 35° and 40°*) and three panel–turbine distances (x=*0.5m, 1.0 and 1.5*). Across all cases, the ENN predictions align closely with the CFD data. In both datasets, C_m decreases with increasing TSR, consistent with the expected aerodynamic behavior of Savonius-type turbines, where torque generation reduces at higher rotational speeds. The small deviations observed between CFD and ENN results remain within acceptable limits, confirming the ENN's capacity to capture the underlying flow dynamics and aerodynamic response of the turbine–panel system. The determination of coefficient R^2=*0.9811* supports this conclusion, indicating a robust linear relationship between the predicted and reference data. Hence, the developed ENN model provides a reliable and computationally efficient means of estimating the torque coefficient across a broad range of geometric and operational conditions.

6.2. The Optimum FNN Model

The performance of the Feedforward Neural Network (FNN) model in predicting the torque coefficient C_m is evaluated using different hidden layer neuron numbers (ranging from 2 to 10), activation functions (*logsig* and *tansig*) and training algorithms (*trainlm* and *trainscg*), as summarized in Table 5. For each configuration, the model's predictive capability is quantified using the MAPE, RMSE and MAE metrics to ensure a robust assessment of accuracy and generalization.

As shown in Table 5, the FNN configuration with the *logsig* activation function, trained using the Levenberg–Marquardt algorithm (*trainlm*) and five neurons in the hidden layer (N=*5*), yielded the most accurate results. Under this configuration, the MAPE, RMSE and MAE values are 3.3583%, 0.0165 and 0.0124, respectively, indicating that the model effectively captures the nonlinear relationships between the input parameters and C_m.

The structure of the optimized FNN model is illustrated in Fig. 17. The network includes four input parameters: tip speed ratio (*TSR*), panel tilt angle (α), panel length (L) and the distance between the panel and the turbine (x). These inputs are connected to a single hidden layer with five neurons (N=*5*). Unlike the Elman Neural Network (ENN), the FNN lacks feedback connections and information flows strictly from the input layer through the hidden layer to the output layer. The output layer produces the predicted torque coefficient C_m for each input configuration.

The predictive accuracy of the FNN model is further assessed through regression analysis, comparing the predicted C_m values against CFD reference data. As shown in Fig. 18, the determination coefficient R^2=*0.9768* indicates a strong agreement between the predicted and actual values, confirming the model's capability to reproduce the aerodynamic behavior of the turbine across the tested range of geometric configurations.

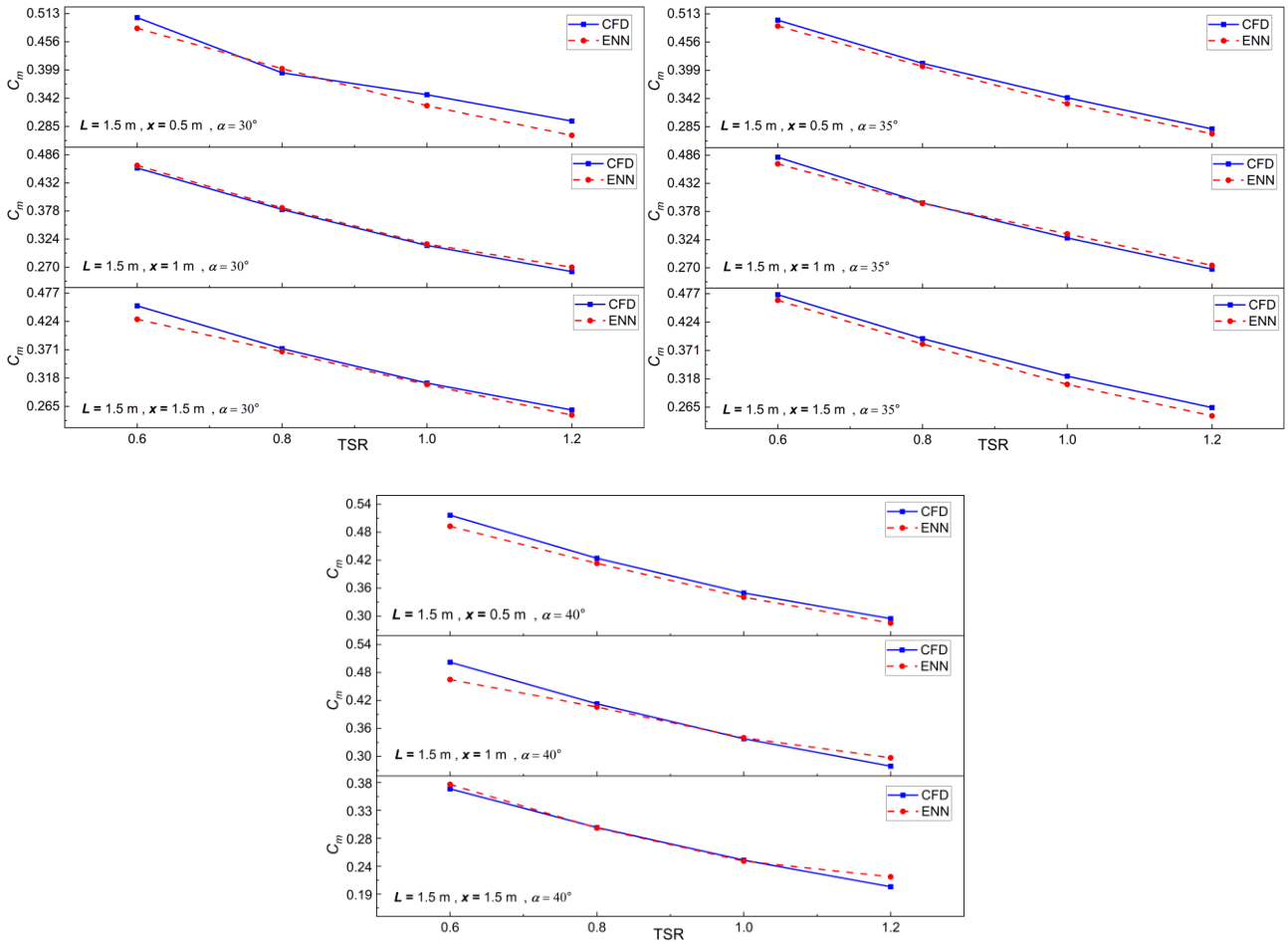


Fig. 16 Comparison of CFD and ENN-predicted C_m values for various panel inclinations (α=30°, 35° and 40°) and distances (x=0.5, 1.0 and 1.5 m) at L=1.5m

Table 5 Performance metrics of various FNN models for C_m prediction

N	MAPE (%)				RMSE				MAE			
	Logsig		Tansig		Logsig		Tansig		Logsig		Tansig	
	trainlm	trainscg	trainlm	trainscg	trainlm	trainscg	trainlm	trainscg	trainlm	trainscg	trainlm	trainscg
2	5.5012	6.7537	5.5007	7.0862	0.0329	0.0315	0.0328	0.0315	0.0175	0.022	0.0172	0.0235
3	5.3329	8.161	5.3407	6.9555	0.0295	0.0364	0.0296	0.0312	0.0167	0.0271	0.0167	0.023
4	3.8155	6.8768	5.5469	6.3636	0.0208	0.0311	0.0263	0.0298	0.0144	0.0226	0.0184	0.0208
5	3.3583	5.6472	5.3358	6.4639	0.0165	0.0252	0.0296	0.0302	0.0124	0.0189	0.0167	0.0211
6	4.7	7.1796	3.9875	5.8164	0.0217	0.0327	0.0182	0.0269	0.015	0.024	0.0136	0.0192
7	4.383	4.9782	10.949	4.7064	0.021	0.0219	0.0568	0.0208	0.0158	0.0177	0.035	0.0161
8	7.2594	3.4679	7.0086	8.0236	0.0337	0.0161	0.0323	0.0343	0.0228	0.0126	0.0256	0.0271
9	7.194	7.861	11.819	8.454	0.0297	0.0374	0.0486	0.04	0.0249	0.0254	0.0391	0.0287
10	8.24	7.054	5.9233	4.8908	0.0313	0.0295	0.0237	0.0238	0.0277	0.0228	0.0195	0.0185

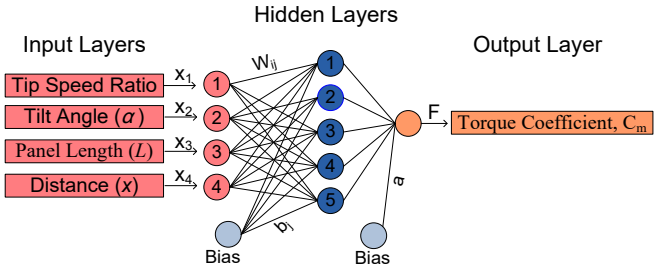


Fig. 17 Architecture of the Feedforward Neural Network (FNN) model developed for C_m prediction

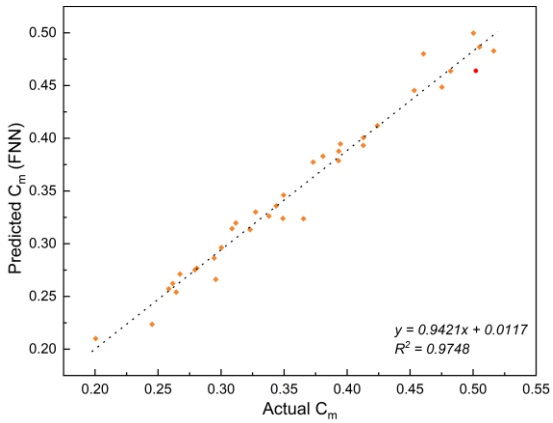


Fig. 18 Regression analysis of predicted versus actual C_m values for the FNN (test dataset)

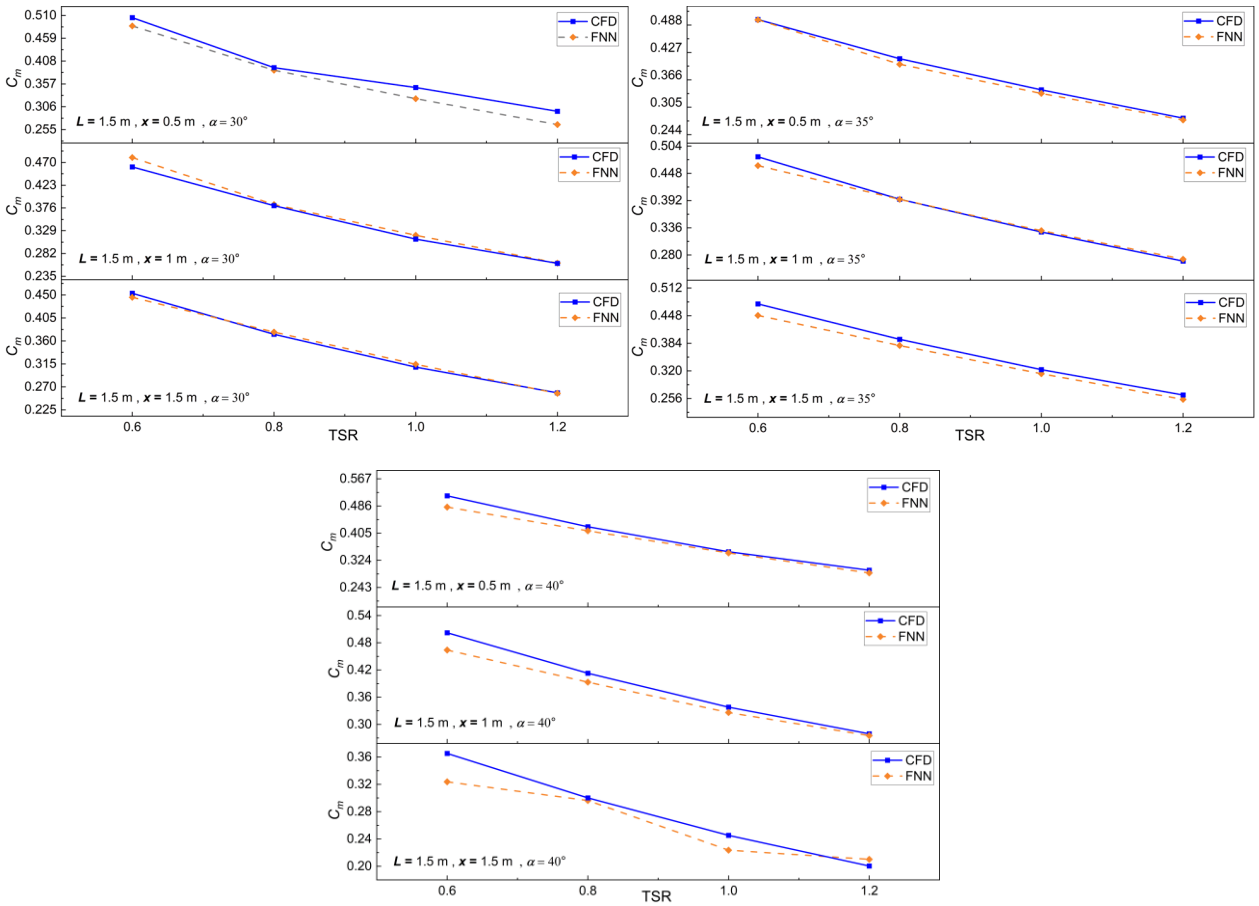


Fig. 19 Comparison of CFD and FNN-predicted C_m values for various panel inclinations (α = 30°, 35°, and 40°) and distances (x = 0.5, 1.0, and 1.5 m) at L = 1.5 m

Table 6 Comparison of optimal ENN and FNN configurations and their error metrics

Model	Optimal Configuration (# of hidden neurons, activation function, training algorithm)	MAPE (%)	RMSE	MAE	R^2
ENN	5 neurons, tansig, trainlm	3.1863	0.014	0.0113	0.9811
FNN	5 neurons, logsig, trainlm	3.3583	0.0165	0.0124	0.9768

Figure 19 compares the FNN-predicted Cm values with the CFD results for a fixed panel length (*L = 1.5 m*), three tilt angles (*α = 30°, 35° and 40°*) and three panel-to-turbine distances (*x =0.5, 1.0 and 1.5 m*). The FNN model accurately captures the decreasing trend of C_m with increasing *TSR*, which is consistent with the expected behavior of Savonius-type turbines. Minor deviations at higher *TSR* values remain within acceptable limits, demonstrating that the FNN model can reliably approximate CFD results for various panel configuration.

Overall, the optimized FNN model provides a computationally efficient and accurate method for predicting turbine torque coefficients. While its feedforward topology lacks the temporal feedback of ENN models, it still effectively captures the main nonlinear relationships among input variables, offering a practical tool for rapid evaluation of panel-turbine configurations.

6.3 Comparative Evaluation of ENN and FNN Models

The comparative performance of the ENN and FNN models in predicting the C_m is presented in Table 6. Both models exhibit strong predictive accuracy, with low error metrics and determination coefficients (R^2) close to 1, confirming their capability to approximate the CFD results effectively. However, subtle differences can be observed in their predictive behavior and generalization characteristics. Although the dataset used in this study is static, the ENN was employed due to its recurrent structure, which enables the representation of correlations between aerodynamic states associated with different geometric and operating conditions. Architectures such as LSTM or GRU were not adopted, as they are primarily intended for time-dependent data. The combined use of FNN and ENN allows a direct and systematic comparison between feedforward and recurrent network architectures in modeling the aerodynamic performance of the hybrid PV–Savonius system.

The ENN achieves the lowest MAPE value of 3.1863 %, together with an RMSE of 0.014 and an MAE of 0.0113, while maintaining a high determination coefficient of R^2=0.9811. In comparison, the FNN yields a MAPE of 3.3583 %, an RMSE of 0.0165, and an MAE of 0.0124, with a slightly lower R^2=0.9768. These results indicate that the ENN provides a modest yet consistent improvement across all error metrics, suggesting enhanced agreement with the CFD reference data.

This improvement is primarily attributed to the ENN's recurrent feedback connections, which enable the network to retain temporal dependencies and represent nonlinear interactions more effectively. Given that the dataset includes multiple geometric and operational variables, namely, the PV-panel tilt angle, panel distance, panel length, and tip-speed ratio (TSR), the ENN's capacity to capture complex multivariable relationships contributes to its superior predictive performance for this configuration-dependent aerodynamic problem.

Figure 20 presents the Taylor diagram comparing both neural models with the CFD test data. The diagram offers an integrated perspective of model performance by simultaneously depicting the correlation coefficient, standard deviation and centered RMSE. As illustrated, the representative point of the ENN lies slightly closer to the reference point on the correlation axis, confirming its stronger correlation and closer alignment with the CFD results. The FNN point, while very close to that of the ENN, is positioned marginally toward the standard-deviation axis, indicating a slightly higher spread in predicted values but still within acceptable limits. The close proximity of both model points to the reference demonstrates that both network structures can reliably reproduce the aerodynamic characteristics of the hybrid turbine system.

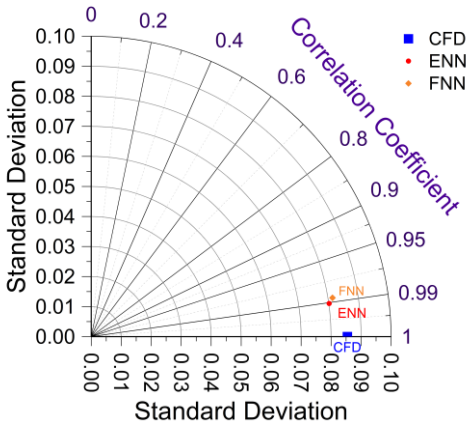


Fig. 20 Taylor diagram comparing the prediction performance of the ENN and FNN models for estimation of C_m

The Taylor diagram also underscores the ENN's ability to achieve a balanced trade-off between variance and correlation, suggesting that its feedback mechanism stabilizes its response while avoiding overfitting to the training data. Conversely, the FNN, characterized by its simpler feedforward topology, ensures efficient learning and stable generalization but lacks the dynamic memory that allows the ENN to capture transient nonlinear interactions with the same precision.

The proposed ANN models demonstrate strong predictive performance within the trained parameter ranges; however, extrapolation beyond these ranges may lead to reduced accuracy, as is typical for data-driven models. For configurations involving significantly different aeroelastic or structural characteristics, such as CFDST wind turbine systems investigated by Li et al. (2025b), additional training data or model re-calibration would be necessary to maintain reliable predictions. Since the ANN models are trained solely on CFD-generated data, their predictive capability is inherently constrained by the underlying CFD assumptions and numerical approximations. As a result, while the models demonstrate strong interpolation accuracy within the simulated parameter space, they may not fully capture real-world variability associated with experimental uncertainties, structural flexibility, or environmental effects.

6.4 Effect of PV Panel Geometric Configuration on Turbine Aerodynamics and Performance

Figure 21 presents the velocity streamlines for various PV panel lengths, distances and angles. The integration of the panel into the flow field significantly modifies the velocity distribution around the Savonius turbine. Certain configurations enhance flow acceleration and direct it toward the turbine, functioning similarly to an airfoil-type deflector (Layeghmand & Tabar, 2020), in agreement with the findings of Lu et al. (2023). In Fig. 21a (L = 2 m, x = 0.5 m, α = 35°), the panel effectively accelerates the flow toward the advancing blade, increasing the torque by promoting a more favorable interaction between the incident flow and the turbine surface (Farajyar et al. 2023). Only a minor portion of the redirected flow passes under the returning blade, thereby minimizing the negative torque contribution.

When the panel length is reduced to L = 1 m (Fig. 21b), the flow-directing effect weakens, even though the panel remains close to the turbine. The shorter panel is unable to guide the accelerated flow efficiently toward the advancing blade, causing a larger portion of the flow to pass beneath the returning blade, thus lowering aerodynamic efficiency compared to other configurations. Conversely, increasing the panel angle to α = 40° with L = 1.5 m (Fig. 21c) produces velocity streamlines similar to those observed in Fig. 21a. Although these two configurations differ in length and angle, their vortex structures and corresponding torque coefficients remain close in value, suggesting that the aerodynamic benefits of the panel can be retained across a range of design variations. In Fig. 21d, where both the panel angle and its distance from the turbine are increased, the flow-directing effect becomes weaker. Examination of the vortex structure in this configuration shows that the formation of a vortex in front of the advancing blade reduces the high-pressure zone in that region. This effect, similar to the deflector-induced pressure modulation observed by Layeghmand et al. (2020), helps lower negative torque. However, since part of the redirected flow bypasses the advancing blade, the overall torque enhancement remains limited compared to the configuration in Fig. 21a. These findings demonstrate that panel placement and geometric parameters are critical for optimizing aerodynamic performance. While an appropriately positioned panel can improve velocity distribution and power generation, excessive spacing or improper orientation can diminish these benefits.

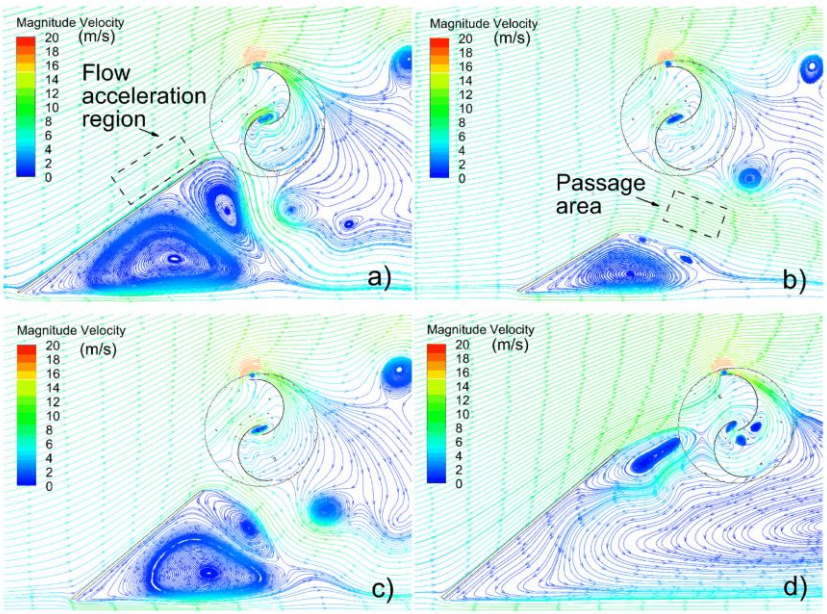


Fig. 21 Velocity streamlines illustrating the effect of PV panel geometry and placement on the flow field around the Savonius turbine at TSR = 1.0: a) L=2 m, x=0.5 m, α=35° b) L=1 m, x=0.5 m, α=30° c) L=1.5 m, x=0.5 m, α=40° d) L=2 m, x=1 m, α=40°

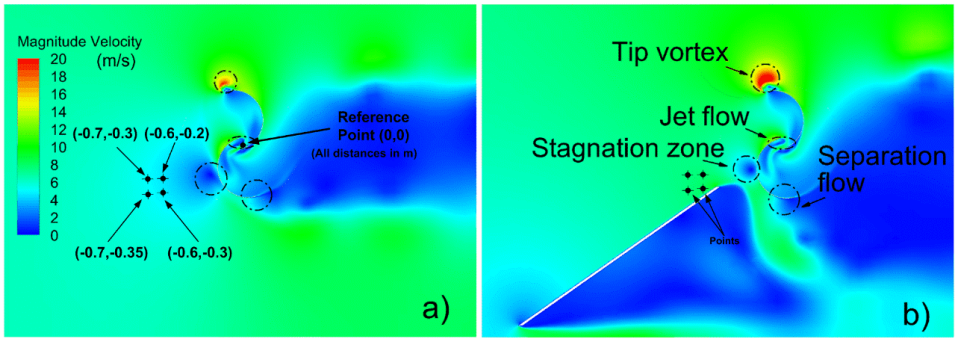


Fig. 22 Instantaneous velocity contours and selected reference points: (a) Savonius turbine without a PV panel, (b) Hybrid configuration with maximum C_m at TSR = 1

In Fig. 22b, the selected optimal configuration demonstrates that the panel effectively guides the flow and increases local velocity around the turbine compared to the baseline Savonius turbine (Fig. 22a). The stagnation region on the convex side of the returning blade is notably smaller than in the classical configuration, indicating reduced negative torque due to redirection of the upstream flow toward the advancing blade (Nimvari et al. 2020). According to Tian et al. (2018) and Layeghmand et al. (2020), tip vortices generated near the advancing blade create a high-velocity region that enhances aerodynamic efficiency. Similarly, the deflector effect in this study promotes these vortices, thereby lowering negative torque by channeling airflow along the convex surface of the returning blade. To quantitatively assess the velocity acceleration induced by the PV panel, reference points with identical coordinates were selected in both the standalone turbine and hybrid configurations. As illustrated in Figs. 22(a) and 22(b), the velocity magnitude increased by 58.8% at the point closest to both the turbine and the panel (x = −0.6, y = −0.3), where the maximum acceleration was observed. This result clearly demonstrates that the incoming flow is significantly accelerated due to the presence of the panel, thereby enhancing the aerodynamic performance of the turbine

The comparison graphs in Fig. 23 illustrate the effect of the PV panel on the torque coefficient (C_m) and power coefficient (Cp). The inclusion of the panel significantly increases both parameters across all TSR values. The higher C_m values indicate improved torque generation resulting from optimized flow interaction, while the corresponding rise in Cp highlights enhanced aerodynamic efficiency. Under the configuration L = 2 m, x = 0.5 m, α = 35°, the maximum power coefficient reaches Cp = 0.3514 at TSR = 1, representing an efficiency improvement of approximately 40.8% compared to the standalone Savonius turbine. These results confirm that the proposed hybrid system, comprising the Savonius turbine and PV panel deflector, achieves clearly higher performance.

Figure 24 illustrates the pressure contours for various panel configurations and their effects on turbine performance. The inclusion of a panel alters the incident flow direction and, consequently, the pressure distribution around the blades. In the absence of a panel (Fig. 24e),

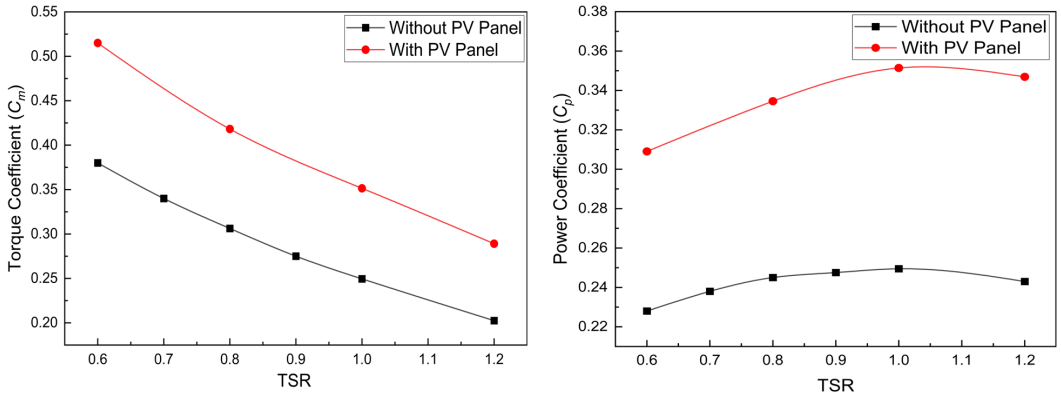


Fig. 23 Comparison of torque coefficient (C_m) and Power Coefficient (C_p) for turbines with and without PV panels

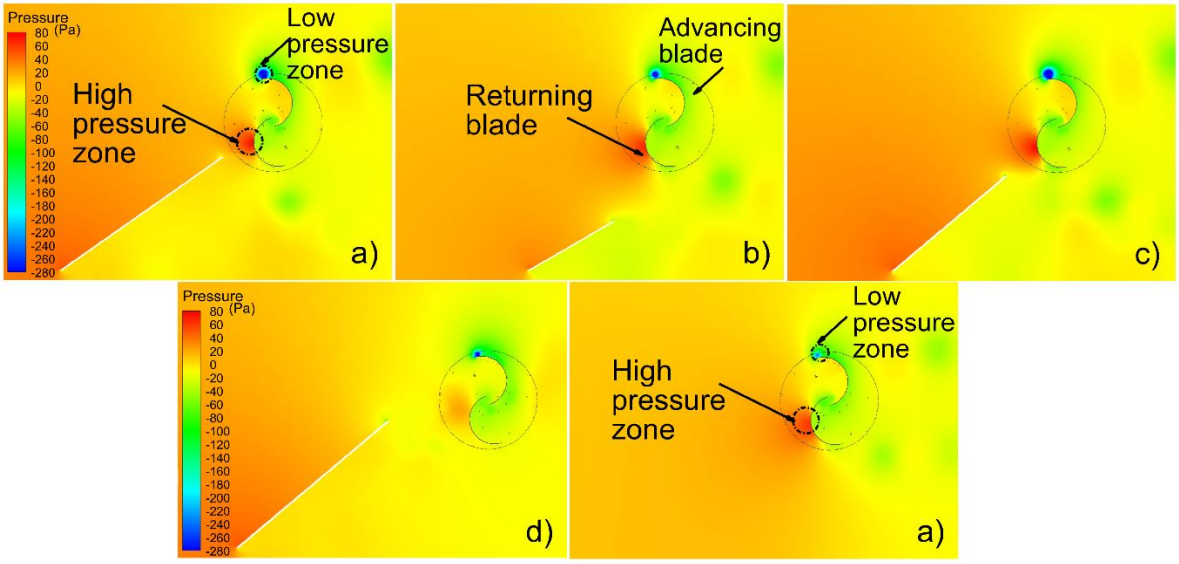


Fig. 24 Pressure contours for different panel lengths, distances and tilt angles at TSR = 1: (a) *L=2 m x=0.5 m α=35°*, (b) *L=1 m x=0.5 m α=30°*, (c) *L=1.5 m x=0.5 m α=40°*, (d) *L=2 m x=1 m α=40°*, (e) Savonious Turbine without panel

the flow directly impacts the convex side of the returning blade, causing considerable momentum loss (Nimvari et al. 2020). When a PV panel acts as a deflector, part of the incoming flow is redirected toward the concave side of the advancing blade, thereby decreasing the high-pressure zone on the convex surface of the returning blade (Fig. 24d) while increasing pressure on the advancing side (Layeghmand et al. 2020).

In configurations with optimal distance and tilt, such as Figs. 24a and 24c, the panel effectively directs the flow, resulting in a higher pressure differential between the two blades. Compared to the no-panel case, the concave side of the advancing blade experiences a greater pressure rise, while the convex side shows a localized pressure reduction, leading to enhanced torque generation (Zhang & Xu, 2024). This pressure asymmetry promotes improved aerodynamic performance and increased C_p values. In contrast, Fig. 24b shows that while the short panel improves the pressure distribution slightly compared to the baseline, it is insufficient to produce a strong flow redirection effect due to its limited length.

In the λ_2 criterion, negative values indicate swirling regions, whereas positive values correspond to shearing region. (Babu & Patel, 2024). In Figs. 25a and 25b, the tip vortex on the advancing blade develops at $\theta = 0^{\circ}$, seperates begins at $\theta = 45^{\circ}$, and the vortex completely detaches from the blade at $\theta = 90°$.Without the panel (Fig. 25a), tip vortices are formed on the returning blade begin to develop 45˚. When the panel is integrated into the system (Fig. 25b), the vortex structures observed on the returning blade are significantly weakened at all angular positions ($\theta = 0^{\circ}$, 45˚, 90˚, and 135˚).

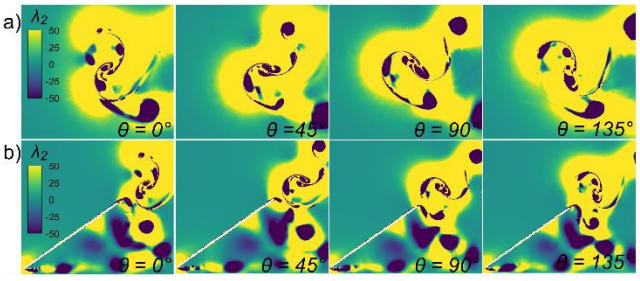


Fig. 25 Contours of the λ_2 criterion illustrating vortex structures: (a) Savonius turbine without PV panel, (b) Savonius turbine with PV panel at L = 2 m, x = 0.5 m, and α = 35°

Instantaneous pressure contours at different azimuthal angles for the configuration yielding the maximum torque coefficient (C_m) in the hybrid system at TSR = 1 are presented in Fig. 26. As shown in Fig. 26(a), a high-pressure region develops on the convex surface of the returning blade, which restricts blade rotation and reduces torque generation (Tian et al. 2018). With the inclusion of the PV panel (Fig. 26(b)), this high-pressure region is significantly reduced, particularly at azimuthal angles of 60° and 120°. For this panel configuration (L = 2 m, x = 0.5 m, α = 35°), the increased pressure difference across the blade surfaces results in a higher net torque, corresponding to a 40.8% increase in the power coefficient (C_p).

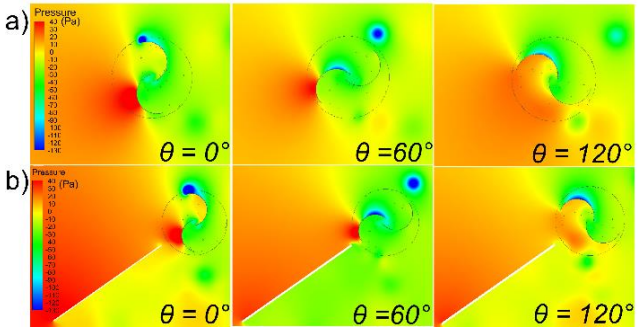


Fig. 26 Instantaneous pressure contours at selected azimuthal angles for (a) Savonius turbine without a PV panel and (b) hybrid configuration with maximum C_m at TSR = 1

Overall, these observations demonstrate that panel distance and tilt angle critically determine the aerodynamic performance of the hybrid system. Properly configured panels enhance the positive torque by creating a strong pressure contrast on the blades, while poorly positioned panels can induce reverse flow zones that reduce efficiency. Therefore, careful optimization of the PV panel geometry is essential for maximizing the aerodynamic performance of Savonius turbines.

7. CONCLUSION

This study presented a comprehensive numerical and data-driven investigation into the aerodynamic performance enhancement of a Savonius-type vertical-axis wind turbine (VAWT) through the integration of photovoltaic (PV) panels acting as flow deflectors. Two-dimensional transient simulations, based on the k–ω SST URANS turbulence model, are performed to analyze the influence of panel geometry and positioning parameters, specifically panel length (L), distance (x) and inclination angle (α), on turbine performance.

The optimal configuration is identified as $L = 2\ m$, $x = 0.5\ m$, and $\alpha = 35°$, yielding a maximum power coefficient of $C_p = 0.3514$ at $TSR = 1$, which represents a 40.8% improvement compared to the standalone Savonius turbine. This significant enhancement was attributed to optimized flow redirection, where the PV panel effectively accelerated the incoming stream toward the advancing blade while reducing the stagnation and negative torque effects on the returning blade. The results demonstrate that properly configured PV panels not only serve as renewable power sources but also act as passive aerodynamic control devices, improving the overall energy conversion efficiency of urban hybrid renewable systems. Although the proposed configuration represents a hybrid PV–Savonius system in terms of physical integration and aerodynamic interaction, the present study is limited to aerodynamic performance evaluation. The electrical power generation of the photovoltaic panel, including the effects of tilt angle on solar irradiance, temperature-induced efficiency losses, shading effects, and structural loading under aerodynamic forces, is not considered. Future studies should therefore focus on a fully coupled hybrid energy assessment by integrating photovoltaic power generation models with wind turbine performance under realistic environmental conditions. Such an approach would enable a comprehensive evaluation of total energy yield, system efficiency, and structural feasibility.

To further extend the aerodynamic assessment and reduce the computational cost of exhaustive CFD simulations, artificial neural network (ANN) models are developed to predict the torque coefficient (C_m) for untested turbine–panel configurations. Among the trained models, the Elman Neural Network (ENN) with five neurons, *tansig* activation, and the *trainlm* algorithm exhibited the highest predictive accuracy, achieving $MAPE = 3.18\%$, $RMSE = 0.014$, $MAE = 0.0113$, and $R^2 = 0.9811$. Its recurrent feedback connections enabled the model to capture temporal and nonlinear flow dependencies more effectively than the conventional Feedforward Neural Network (FNN), which, although competitive ($MAPE = 3.36\%$), showed slightly lower generalization capability.

The findings confirm that the ENN-based predictive framework offers a robust, computationally efficient and time-saving alternative to transient CFD simulations. By accurately reproducing aerodynamic performance metrics across varying configurations, the proposed hybrid CFD–ENN methodology enables rapid design exploration and optimization of PV-assisted VAWT systems.

The key outcomes and contributions of this study can be summarized as follows:

- Demonstration of the aerodynamic benefit of integrating PV panels serving simultaneously as renewable power elements and aerodynamic deflectors.
- Identification of the optimum hybrid configuration ($L = 2\ m$, $x = 0.5\ m$, $\alpha = 35°$), which improved turbine efficiency by 40.8% compared with the standalone Savonius design.
- Development and validation of ANN-based predictive models (ENN and FNN) capable of accurately estimating torque coefficients with minimal error, thereby reducing reliance on extensive CFD simulations.
- Confirmation of the superior predictive capability of the ENN, highlighting its effectiveness in capturing temporal nonlinear aerodynamic interactions.

- Provision of a computationally efficient framework for aerodynamic performance prediction and parameter optimization of hybrid PV–wind turbine systems.

Overall, the findings confirm that the proposed hybrid configuration enhances both aerodynamic and energy conversion performance while offering a feasible and multifunctional design approach for future renewable energy systems. From a practical perspective, the positioning and configuration of the PV panels may introduce structural constraints and installation challenges, as well as potential trade-offs between aerodynamic performance enhancement and photovoltaic efficiency. These aspects were beyond the scope of the present aerodynamic-focused study and should be addressed in future work through coupled aerodynamic–structural analyses and experimental investigations. The developed ENN-based predictive framework provides a robust tool for accelerating design evaluation, facilitating optimization studies, and guiding experimental validation within defined parameter ranges in future research.

CONFLICT OF INTEREST

The authors confirm that they have no financial, commercial, or personal relationships that could be perceived as a potential conflict of interest regarding the research and publication of this study.

AUTHOR CONTRIBUTIONS

Melisa Yilmaz: AI modeling, Methodology, CFD simulations, Writing – Original Draft; **Yasin Mehmet Yilmaz:** Methodology, Data Analysis, Visualization,CFD simulations, Writing – Original Draft; **Hakan Yavuz:** Supervision, Critical Feedback on Study Design,AI modeling and Methodology, Review & Editing.

REFERENCES

Aboujaoude, H., Beaumont, F., Murer, S., Polidori, G., & Bogard, F. (2022). Aerodynamic performance enhancement of a Savonius wind turbine using an axisymmetric deflector. *Journal of Wind Engineering and Industrial Aerodynamics*, *217*, 104882. https://doi.org/10.1016/j.jweia.2021.104882

Akbıyık, H., & Yavuz, H. (2021). Artificial neural network application for aerodynamics of an airfoil equipped with plasma actuators. *Journal of Applied Fluid Mechanics*, *14*(4), 1165–1181. https://doi.org/10.47176/jafm.14.04.32133

Akwa, J. V., Vielmo, H. A., & Petry, A. P. (2012). A review on the performance of Savonius wind turbines. *Renewable and Sustainable Energy Reviews*, *16*(5), 3054–3064. https://doi.org/10.1016/j.rser.2012.02.056

Al-Ghriybah, M., Zulkafli, M. F., Didane, D. H., & Mohd, S. (2021). The effect of spacing between inner blades on the performance of the Savonius wind turbine. *Sustainable Energy Technologies and Assessments*, *43*, 100988. https://doi.org/10.1016/j.seta.2020.100988

Altan, B. D., & Atılgan, M. (2010). The use of a curtain design to increase the performance level of a Savonius wind rotors. *Renewable Energy*, *35*(4), 821–829. https://doi.org/10.1016/j.renene.2009.08.025

Babu, G. V., & Patel, D. K. (2024). Effect of semi-elliptical outer blade-surface on the Savonius hydrokinetic turbine performance: A numerical investigation. *Journal of Applied Fluid Mechanics*, *17*(4), 828–843. https://doi.org/10.47176/jafm.17.4.2235.

Bai, H. L., Chan, C. M., Zhu, X. M., & Li, K. M. (2019). A numerical study on the performance of a Savonius-type vertical-axis wind turbine in a confined long channel. *Renewable Energy*, *139*, 102–109. https://doi.org/10.1016/j.renene.2019.02.044

Duc, M. B., The H. T., Van, K. P., & Le, A. D. (2023) Predicting aerodynamic performance of Savonius wind turbine: An application of generalized k–ω turbulence model.*Ocean Engineering*, *286*, 115690. https://doi.org/10.1016/j.oceaneng.2023.115690

Bilgili, M., Ozbek, A., Yildirim, A., & Simsek, E. (2023). Artificial neural network approach for monthly air temperature estimations and maps. *Journal of Atmospheric and Solar–Terrestrial Physics*, *242*, 106000. https://doi.org/10.1016/j.jastp.2022.106000

Biswas, A. Sarkar, S., & Gupta, R. (2016). Application of artificial neural network for performance evaluation of vertical axis wind turbine rotor. *International Journal of Ambient Energy, 37*(2), 209–218. http://dx.doi.org/10.1080/01430750.2014.915889

Çakmak, Z. (2024). An overview of Türkiye's renewable energy outlook. *Mühendis ve Makina / Engineer and Machinery*, *65*(717), 558–597. https://doi.org/10.46399/muhendismakina.1599383

Chai, T., & Draxler, R. R. (2014). Root mean square error (RMSE) or mean absolute error (MAE)? Arguments against avoiding RMSE in the literature. *Geoscientific Model Development*, *7*(3), 1247–1250. https://doi.org/10.5194/gmd-7-1247-2014

Chandra, R., & Zhang, M. (2012). Cooperative coevolution of Elman recurrent neural networks for chaotic time series prediction. *Neurocomputing*, *86*, 116–123. https://doi.org/10.1016/j.neucom.2012.01.014

Cacciola, M., Megali, G., Pellicano, D., & Morabito, F. C. (2012). Elman neural networks for characterizing voids in welded strips: A study. *Neural Computing and Applications*, *21*, 869–875. https://doi.org/10.1007/s00521-011-0609-3

Debnath, B. K., & Das, R. (2010). Prediction of performance coefficients of a three-bucket Savonius rotor using artificial neural network. *Journal of Renewable and Sustainable Energy, 2* (4), 043107https://doi.org/10.1063/1.3467510

Dewan, A., Gautam, A., & Goyal, R. (2021). Savonius wind turbines: A review of recent advances in design and performance enhancements. *Materials Today: Proceedings. 47,* 2976-2983 https://doi.org/10.1016/j.matpr.2021.05.205

Deye ESS (2025, July 21). Guide to solar panel sizes and dimensions. Retrieved October 30, 2025, from https://deyeess.com/guide-to-solar-panel-sizes-and-dimensions/

Enerji, A. (2025, September). Türkiye'nin kurulu gücü [Installed capacity of Türkiye]. Retrieved October 30, 2025, from https://enerjiajansi.com.tr/turkiyenin-kurulu-gucu/

Farajyar, S., Ghafoorian, F., Mehrpooya, M., & Asadbeigi, M. (2023). CFD investigation and optimization on the aerodynamic performance of a Savonius vertical axis wind turbine and its installation in a hybrid power supply system: A case study in Iran. *Sustainability*, *15*(6), 5318. https://doi.org/10.3390/su15065318

Ferrari, G., Federici, D., Schito, P., Inzoli, F., & Mereu, R. (2017). CFD study of Savonius wind turbine: 3D model validation and parametric analysis. *Renewable Energy*, *105*, 722–734. https://doi.org/10.1016/j.renene.2016.12.077

Ghorbani, M. A., Khatibi, R., Hosseini, B., & Bilgili, M. (2013). Relative importance of parameters affecting wind speed prediction using artificial neural networks. *Theoretical and Applied Climatology*, *114*, 107–114. https://doi.org/10.1007/s00704-012-0821-9

Ghorbani, M. A., Shamshirband, S., Haghi, D. Z., Azani, A., Bonakdari, H., & Ebtehaj, I. (2017). Application of firefly algorithm-based support vector machines for prediction of field capacity and permanent wilting point. *Soil & Tillage Research*, *172*, 32–38. https://doi.org/10.1016/J.STILL.2017.04.009

Golecha, K., Eldho, T. I., & Prabhu, S. V. (2011). Influence of the deflector plate on the performance of modified Savonius water turbine. *Applied Energy*, *88*(9), 3207–3217. https://doi.org/10.1016/j.apenergy.2011.03.025

Guo, F., Song, B., Mao, Z., & Tian, W. (2020). Experimental and numerical validation of the influence on Savonius turbine caused by rear deflector. *Energy, 196*, 117132. https://doi.org/10.1016/j.energy.2020.117132

Harsito, C., Tjahjana, D. D. D. P., & Kristiawan, B. (2020). Savonius turbine performance with slotted blades. *AIP Conference Proceedings*, *2217*, 030071. https://doi.org/10.1063/5.0000797

Ingole, A. S., & Rakhonde, B. S. (2015). Hybrid power generation system using wind energy and solar energy. *International Journal of Scientific and Research Publications*, *5*(3). Retrieved from http://www.ijsrp.org/research-paper-0315.php?rp=P393854

Institute for Energy Economics & Financial Analysis (IEEFA). (2019, December 19). *Turkey turns to solar power to boost energy independence*. Retrieved October 30, 2025, from https://ieefa.org/articles/ieefa-report-turkey-turns-solar-power-boost-energy-independence

Jha, S. K., Bilalovic, J., Jha, A., Patel, N. & Zhang, H. (2017). Renewable energy: Present research and future scope of artificial intelligence. *Renewable and Sustainable Energy Reviews*, *77*, 297-317. https://doi.org/10.1016/j.rser.2017.04.018

Kacira, M., Simsek, M., Babur, Y., & Demirkol, S. (2004). Determining optimum tilt angles and orientations of photovoltaic panels in Sanliurfa, Turkey. *Renewable Energy*, *29*(8), 1265-1275. https://doi.org/10.1016/j.renene.2003.12.014.

Karimian, S. M. H., & Abdolahifar, A. (2020). Performance investigation of a new Darrieus vertical axis wind turbine. *Energy*, *191*, 116551. https://doi.org/10.1016/j.energy.2019.116551

Kut, P., & Pietrucha-Urbanik, K. (2024). Bibliometric analysis of renewable energy research on the example of the two European countries: *Insights, challenges, and future prospects. Energies*, *17*(1), 176. https://doi.org/10.3390/en17010176

Layeghmand, K., Tabar, N. G., & Zarkesh, M. (2020). Improving efficiency of Savonius wind turbine by means of an airfoil-shaped deflector. *Journal of the Brazilian Society of Mechanical Sciences and Engineering*, *42*, 528. https://doi.org/10.1007/s40430-020-02598-7

Lee, B., Trcka, M., & Hensen, J. L. M. (2014). Rooftop photovoltaic (PV) systems: A cost–benefit analysis study of industrial halls. *International Journal of Low-Carbon Technologies*, *9*(4), 285–297. https://doi.org/10.1093/ijlct/ctt008

Li, D., Sang, Y., Lv, Z., Wu, K., & Lai, Z. (2025a). Dynamic response analysis of wind turbine tower with high aspect ratio: Wind tunnel tests and CFD simulation. *Thin-Walled Structures, 211*, 113113. https://doi.org/10.1016/j.tws.2025.113113

Li, D., Fang, S., Sun, C., Xu, F., Zhao, J., & Lai, Z. (2025b). Aeroelastic wind tunnel study and numerical simulation of Concrete-Filled Double-Skin Tubular (CFDST) wind turbine system. *Structures, 74*, 108581. https://doi.org/10.1016/j.istruc.2025.108581.

Lu, H., Zhou, L., Wen, J., Tang, H., Guo, P., Tse, T. K. T., & Zhang, H. (2023). Aerodynamic performance improvements for a Savonius turbine above a forward-facing step via inclined solar panel: A computational study. *Journal of Cleaner Production*, *413*, 137413. https://doi.org/10.1016/j.jclepro.2023.137413

Mohamed, M. H., Janiga, G., Pap, E., & Thévenin, D. (2010). Optimization of Savonius turbines using an obstacle shielding the returning blade. *Renewable Energy, 35*(11), 2618–2626. https://doi.org/10.1016/j.renene.2010.04.007

Mohamed, M. H., Janiga, G., Pap, E., & Thévenin, D. (2011). Optimal blade shape of a modified Savonius turbine using an obstacle shielding the returning blade. *Energy Conversion and Management*, *52*(1), 236–242. https://doi.org/10.1016/j.enconman.2010.06.070

Mohammadi, M., Lakestani, M., & Mohamed, M. H. (2018). Intelligent parameter optimization of Savonius rotor using artificial neural network and genetic algorithm. *Energy*, *143*, 56-68. https://doi.org/10.1016/j.energy.2017.10.121

Nimvari, M. E., Fatahian, H., & Fatahian, E. (2020). Performance improvement of a Savonius vertical axis wind turbine using a porous deflector. *Energy Conversion and Management*, *220*, 113062. https://doi.org/10.1016/j.enconman.2020.113062

Noman, A. A.,Tasneem Z., Abhi S. H., Badal F. R., Rafsanzane M., Islam M. R. & Alam F. (2023). Savonius wind turbine blade design and performance evaluation using ANN-based virtual clone: A new approach. *Heliyon*, *9*(5), e15672. https://doi.org/10.1016/j.heliyon.2023.e15672

Ozturk, I. (2013). Energy dependency and energy security: The role of energy efficiency and renewable energy sources (The Mahbub Ul Haq Memorial Lecture). *The Pakistan Development Review*, *52*(4), 309–330. https://doi.org/10.30541/V52I4IPP.309-330

Rathod, U. H., Kulkarni V. & Saha U. K. (2021). On the application of machine learning in Savonius wind turbine technology: An estimation of turbine performance using artificial neural network and genetic expression programming. *Journal of Energy Resources Technology*, *144*(6), 061301.https://doi.org/10.1115/1.4051736

Rizk, M., & Nasr, K. (2023). Computational fluid dynamics investigations over conventional and modified Savonius wind turbines. *Heliyon*, *9*(6), e16876. https://doi.org/10.1016/j.heliyon.2023.e16876

Sagharichi, A., Zamani, M., & Ghasemi, A. (2018). Effect of solidity on the performance of variable-pitch vertical axis wind turbine. *Energy*, *161*, 753–775. https://doi.org/10.1016/j.energy.2018.07.160

Sanaye, S., Yazdani, S., & Farvizi, A. (2025). Optimizing a straight-bladed vertical axis wind turbine with computational fluid dynamics (CFD), artificial neural network (ANN), and genetic algorithm (GA). *Energy Science & Engineering*, *13*(12), https://doi.org/10.1002/ese3.70289

Sharma, S., & Sharma, R. K. (2016). Performance improvement of Savonius rotor using multiple quarter blades – A CFD investigation. *Energy Conversion and Management*, *127*, 43–54. https://doi.org/10.1016/j.enconman.2016.08.087

Sheldahl, R. E., Blackwell, B. F., & Feltz, L. V. (1978). Wind tunnel performance data for two- and three-bucket Savonius rotors. *Journal of Energy, 2*(3), 160–164. https://doi.org/10.2514/3.47966

Sims, R. E. H., Rogner, H. H., & Gregory, K. (2003). Carbon emission and mitigation cost comparisons between fossil fuel, nuclear and renewable energy resources for electricity generation. *Energy Policy*, *31*(13), 1315–1326. https://doi.org/10.1016/S0301-4215(02)00192-1

Storti, B. A., Dorella J. J., Roman N. D., Peralta I. & Albanesi A. E. (2019). Improving the efficiency of a Savonius wind turbine by designing a set of deflector plates with a metamodel-based optimization approach. *Energy*, *186*, 115814 https://doi.org/10.1016/j.energy.2019.07.144

Sobhani, E., Ghaffari, M., & Maghrebi, M. J. (2017). Numerical investigation of dimple effects on Darrieus vertical axis wind turbine. *Energy*, *133*, 231–241. https://doi.org/10.1016/j.energy.2017.05.105

Tartuferi, M., D'Alessandro, V., Montelpare, S., & Ricci, R. (2015). Enhancement of Savonius wind rotor aerodynamic performance: A computational study of new blade shapes and curtain systems. *Energy*, *79*, 371–384. https://doi.org/10.1016/j.energy.2014.11.023

Tian, W., Mao, Z., Zhang, B., & Li, Y. (2018). Shape optimization of a Savonius wind rotor with different convex and concave sides. *Renewable Energy, 117*, 287–299. https://doi.org/10.1016/j.renene.2017.10.067

Tümse, S., İlhan, A., Bilgili, M., & Şahin, B. (2022a). Estimation of wind turbine output power using soft computing models. *Energy Sources, Part A: Recovery, Utilization, and Environmental Effects, 44*(2), 3757–3786. https://doi.org/10.1080/15567036.2022.2066226

Tümse, S., Bilgili, M., & Sahin, B. (2022b). Estimation of aerodynamic coefficients of a non-slender delta wing under ground effect using artificial intelligence techniques. *Neural Computing and Applications*, *34*, 10823–10844. https://doi.org/10.1007/s00521-022-07013-x

Udochukwu, I. S., & Innocent, A. E. (2024). The role of renewable energy in combating climate change: Progress and challenges. *International Journal of Research and Innovation in Social Science*, *8*(10), 3096-3103. https://doi.org/10.47772/IJRISS.2024.8100260

Ünal, Ş., Bilgili, M., Büyükalaca, O., & Akgün, H. (2025). Development of an artificial intelligence-based cooling load map for buses in Türkiye. *Thermal Science and Engineering Progress*, *61*, 103516. https://doi.org/10.1016/j.tsep.2025.103516

Wenehenubun, F., Saputra, A., & Sutanto, H. (2015). An experimental study on the performance of Savonius wind turbines related with the number of blades. *Energy Procedia*, *68*, 297–304. https://doi.org/10.1016/j.egypro.2015.03.259

Willmott, C. J., & Matsuura, K. (2005). Advantages of the mean absolute error (MAE) over the root mean square error (RMSE) in assessing average model

performance. *Climate Research, 30*, 79–82. https://doi.org/10.3354/cr030079

World Map Wallpapers. (2025). World map wallpapers. Retrieved October 30, 2025, from https://wallpapercg.com/world-map-wallpapers

Yadav, A. K., & Chandel, S. S. (2013). Tilt angle optimization to maximize incident solar radiation: A review, Renewable and Sustainable Energy Reviews, *23*, 503-513. https://doi.org/10.1016/j.rser.2013.02.027.

Yüzer, E. Ö. (2023, July 29–31). A review of the development of solar energy capacity in Turkey. In *Proceedings of the 1st International Conference on Modern and Advanced Research (ICMAR)*, Konya, Turkey. (pp. 63 - 69). All Sciences Proceedings. https://doi.org/10.59287/icmar.1257

Zhang, T., & Xu, S. (2024). A novel wind energy gathering structure for the Savonius wind turbine and its parameter optimization based on Taguchi's method. *Energies*, *17*(21), 5348. https://doi.org/10.3390/en17215348

Zohuri, B. (2017). Hybrid renewable energy systems (pp. 1–38). *In Hybrid energy systems (pp. 1–32). Springer*. https://doi.org/10.1007/978-3-319-70721-1_1